J. Fluid Mech. (2014), *vol.* 760, *pp.* 63–94. © Cambridge University Press 2014
doi:10.1017/jfm.2014.591

The influence of harmonic wall motion on transitional boundary layers

M. J. Philipp Hack[1] **and Tamer A. Zaki**[1,†]

[1]Department of Mechanical Engineering, Imperial College London, London SW7 2AZ, UK

(Received 12 March 2014; revised 8 August 2014; accepted 5 October 2014)

The influence of harmonic spanwise wall motion on bypass transition in boundary layers is investigated using direct numerical simulations. It is shown that the appropriate choice of the forcing parameters can achieve a substantial stabilization of the laminar flow regime. However, an increase of the forcing amplitude or period beyond their optimal values diminishes the stabilizing effect, and leads to breakdown upstream of the unforced case. For the optimal wall-oscillation parameters, the reduction in propulsion power substantially outweighs the power requirement of the forcing. The mechanism of transition delay is examined in detail. Analysis of the pre-transitional streaks shows that the wall oscillation substantially reduces their average amplitude, and eliminates the most energetic streaks. As a result, the secondary instabilities that precede breakdown to turbulence are substantially weakened – an effect demonstrated by linear stability analyses of flow fields from direct numerical simulations. The outcome is transition delay owing to a significant reduction in the frequency of occurrence of turbulent spots and a downstream shift in their average inception location. Finally, it is shown that the efficiency of the forcing can be further improved by replacing the sinusoidal time dependence of the wall oscillation with a square wave.

Key words: boundary layer stability, transition to turbulence

1. Introduction

Transition to turbulence in boundary layers is promoted in the presence of external perturbations. In such conditions, the relatively slow natural transition process is bypassed. The final state is a turbulent boundary layer and therefore a higher level of viscous drag. Earlier works have devoted considerable efforts towards the reduction of the high skin friction of the turbulent regime. These studies established the effectiveness of transverse, time-harmonic wall forcing in decreasing wall friction in fully turbulent flows. The present work investigates the influence of such forcing on bypass transition in boundary layers beneath free-stream turbulence.

---

† Present address: Department of Mechanical Engineering, Johns Hopkins University, Baltimore, MD 21218, USA. Email address for correspondence: t.zaki@jhu.edu

1.1. *Bypass transition in boundary layers*

Boundary layer transition to turbulence may be described as a succession of receptivity to external disturbances, growth of primary and secondary instabilities and finally nonlinear breakdown. Two classes of transition have been defined, based on the nature of the primary perturbations. The prevalence of either mechanism, and thus the observed variant of the transition process, largely depends on the spectrum of the initial perturbation field (see e.g. Arnal & Michel 1990; Saric, Reed & Kerschen 2002).

The first breakdown scenario is commonly known as natural transition and arises in the presence of small-amplitude background perturbations (e.g. Kleiser & Zang 1991). This route to turbulence is characterized by the exponential amplification of discrete instability modes, or Tollmien–Schlichting waves, above the critical Reynolds number. At some distance downstream, these two-dimensional waves reach levels of the order of several per cent of the free-stream velocity. At this point, the flow becomes susceptible to three-dimensional secondary instabilities (e.g. Herbert 1988). The subsequent breakdown occurs through the formation of localized turbulent spots (Emmons 1951), which grow in extent and eventually merge to form a continuous turbulent region.

The second class, known as bypass transition, refers to breakdown scenarios that deviate from the above description (see e.g. the reviews by Durbin & Wu (2007) and Zaki (2013)). Initial disturbance growth is dominated by algebraic, or non-modal, amplification, which is active at all Reynolds numbers. The bypass process thus describes a potentially faster path to turbulence than the Tollmien–Schlichting mechanism. Algebraic growth is nevertheless transient and is overcome by viscous decay at finite time. Hence, only perturbations with significant initial magnitude can amplify via the non-modal mechanism and reach sufficient levels to promote laminar–turbulent transition. Studies by Suder, O'Brien & Reshotko (1981) established an initial perturbation amplitude between 0.5 and 1 % as a lower bound for algebraic growth to become the dominant primary amplification mechanism.

While other disturbances such as surface roughness and acoustic waves are potential sources for bypass breakdown, the term 'bypass' is commonly associated with transition caused by free-stream vortical perturbations. The bypass process therefore requires a mechanism that allows these external disturbances to enter the boundary layer. Rapid distortion theory (Hunt & Carruthers 1990; Hunt & Durbin 1999) and inviscid receptivity studies (Kerschen 1991) demonstrated that regions of mean shear are shielded from external vortical perturbations – a phenomenon referred to as 'shear sheltering'. In the presence of viscosity, low-frequency perturbations nonetheless enter the shear (Jacobs & Durbin 1998). This can be explained using a model problem that compares the diffusive time scale for external vortical perturbations to penetrate the boundary layer and the shear time scale (Zaki & Saha 2009).

Low-frequency vortical disturbances that penetrate the shear trigger a response inside the boundary layer. For example, it was discovered by Dryden (1936) that external perturbations with amplitudes of the order of a few per cent of the free-stream velocity cause laminar boundary layers to develop 'speed fluctuations of amplitude considerably greater than that in the free stream'. Taylor (1939) reported the very low frequency of these streaky perturbations, which are dominated by the streamwise velocity component. The works by Klebanoff, Tidstrom & Sargent (1962) and Klebanoff (1971) later brought broader attention to these 'breathing modes', which the authors had termed accordingly because of their thinning and thickening effect on the boundary layer. In recognition of these earlier contributions, Kendall

(1985) established the now common terminology of ‘Klebanoff modes’. It should be noted that these ‘modes’ are not eigenfunctions of the governing equations, even though elongated structures like streaks can be considered a general property of shear layers (Phillips 1969).

Landahl (1975, 1980) explained the origin of streaks in terms of the vertical displacement of mean momentum. This so-called lift-up effect ultimately results from the action of wall-normal velocity perturbations with finite spanwise wavelength on the mean shear of the boundary layer. As a consequence, the mean shear is tilted, which causes the production of normal vorticity and thus a perturbation in the streamwise velocity component. Three-dimensional wall-normal velocity perturbations alone are therefore sufficient for the generation of Klebanoff streaks (see e.g. Breuer & Haritonidis 1990; Leib, Wundrow & Goldstein 1999). Optimal growth studies (Butler & Farrell 1992; Andersson, Berggren & Henningson 1999) demonstrated that the optimal spanwise perturbation wavelength is of the order of the local boundary-layer thickness.

Low-frequency streaks, however, do not immediately initiate breakdown. Rather, the regions of increased shear that surround these primary features provide the potential for the development of high-frequency secondary instabilities. Two modes of instabilities are possible (Vaughan & Zaki 2011; Hack & Zaki 2014). Outer modes are situated on top of boundary-layer streaks and were the dominant type of instability in a number of studies (Jacobs & Durbin 2001; Brandt, Schlatter & Henningson 2004; Zaki & Durbin 2005). Inner modes become more relevant in the presence of adverse pressure gradients. Beyond the initial growth of the secondary instability, full nonlinear breakdown to turbulence is observed. The resulting spots have opening angles between 18 and 20°, consistent with theoretical (Bowles & Smith 1995) and experimental studies (Wygnanski, Sokolov & Friedman 1976; Chong & Zhong 2005).

1.2. *Reduction of turbulent drag by unsteady forcing*

For a given Reynolds number, the skin friction of fully turbulent flow is considerably higher than for laminar conditions. An attempt to reduce drag can focus on altering the turbulent state or on delaying the onset of turbulence. In the former category, one mechanism that has received considerable attention is spanwise wall oscillation. The effectiveness of the same mechanism to stabilize the laminar flow regime, and thus delay the onset of turbulence, is examined herein. Therefore, a discussion of the efforts in the context of fully turbulent flow is presented first, followed by some recent efforts in the field of transition delay.

The experimental investigations by Bradshaw & Pontikos (1985) showed a significant decrease in turbulent skin friction as the transverse pressure gradient along a swept wing rapidly changed the direction of the mean flow. Driver & Hebbar (1987) and Spalart (1989) investigated three-dimensional turbulent boundary layers with continuously changing mean flow direction and noted that the formation of streak-like elongated structures is largely suppressed. In internal flows, Moin *et al.* (1990) performed direct numerical simulations (DNS) of channel flow subjected to an impulsively started spanwise pressure gradient. They demonstrated a substantial reduction in the turbulence kinetic energy as the mean flow became strongly three-dimensional. Once the base flow realigned itself in the new direction and became two-dimensional again, the kinetic energy recovered its original level. Jung, Mangiavacchi & Akhavan (1992) simulated turbulent channel flow with spanwise wall oscillation. They demonstrated the continuous reduction of the mean wall shear stress for oscillation periods $25 < T^+ < 200$, where $T^+ = Tu_\tau^2/\nu$ and u_τ is the friction velocity.

Baron & Quadrio (1996) investigated the energy budget for oscillatory wall forcing applied to turbulent channel flow. It was shown that the energy savings that result from a reduction in turbulent drag may, for suitable choice of parameters, outweigh the power input into the oscillatory movement so that a net energetic gain is achieved. A comprehensive review of turbulent flows under the influence of transverse forcing is given by Karniadakis & Choi (2003). Further contributions by Choi (2002) related the reduction in turbulent skin friction to the weakening of sweep events, in which high-speed fluid is transported towards the wall. Quadrio & Ricco (2004) established a characteristic quantity S, which is linearly correlated with drag reduction in turbulent channel flow for a wide range of forcing parameters. More recently, Quadrio, Ricco & Viotti (2009) and Viotti, Quadrio & Luchini (2009) investigated the effect of wall forcing in the form of steady and travelling streamwise waves. The comprehensive study by Touber & Leschziner (2012) focused on the impact of oscillatory wall forcing on turbulent streaks. The authors concluded that intervals of the oscillation cycle during which the shear changes slowly weaken the overall drag reduction effect. They assert that these phases allow the turbulent streaks sufficient time to grow in the instantaneous direction of the shear vector.

The above literature focused on the influence of wall oscillation on turbulent flows. In comparison, relatively little is known regarding the efficacy of wall forcing to influence transition to turbulence in boundary layers. Experimental studies of transition delay have largely focused on wall suction (Fransson & Alfredsson 2003) and compliant surfaces (Huang & Johnson 2007). Another approach attempted to exploit streaks in order to delay natural transition. Experiments by Boiko *et al.* (1994) and Fransson *et al.* (2005) showed that the presence of Klebanoff streaks can weaken the amplification of the primary Tollmien–Schlichting waves. The underlying mechanism was attributed to a negative production term associated with the spanwise variation of the streaky base state (Cossu & Brandt 2004). It should be noted, however, that the streaks can also promote transition by enhancing the secondary instability of Tollmien–Schlichting waves (Liu, Zaki & Durbin 2008*a*,*b*). More recent attempts to delay transition include the work by Duchmann, Grundmann & Tropea (2013). They demonstrated the effectiveness of dielectric barrier discharges to increase the Reynolds number at the onset of natural transition by approximately 10 %. Hanson *et al.* (2014) used a closed-loop control set-up with plasma actuators to attenuate streaks in pre-transitional boundary layers. Furthermore, a number of theoretical studies demonstrated a weakening of the lift-up mechanism for different flow configurations, for example viscosity stratification (Sameen & Govindarajan 2007), two-fluid flows (Malik & Hooper 2005) and steady spanwise wall forcing (Ricco 2011).

The present work investigates the effect of a spanwise oscillatory wall motion on bypass transition using DNS. A description of the simulation set-up and the computational method is given in § 2. Section 3 reports integral measures of the effect of the wall forcing on the bypass process. Section 4 is devoted to the lift-up mechanism and boundary-layer streaks, while § 5 focuses on the secondary instabilities and the subsequent breakdown to turbulence. Finally, § 6 discusses the effect of varying the forcing amplitude and waveform.

2. Simulation set-up

The numerical method solves the full incompressible Navier–Stokes equations using the fractional step algorithm by Kim & Moin (1985). The equations are discretized

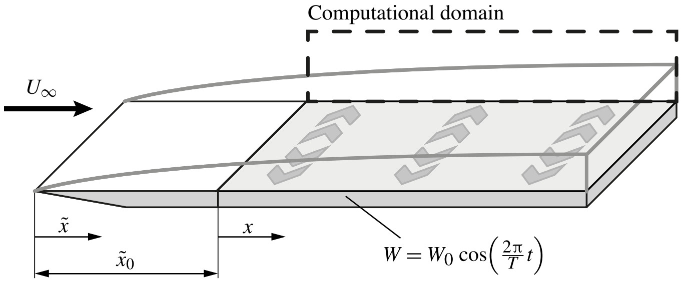

FIGURE 1. Schematic of the computational domain.

with the finite-volume approach described by Rosenfeld, Kwak & Vinokur (1991). The convective terms are advanced in time using an explicit Adams–Bashforth scheme, and the diffusion terms are treated implicitly with a Crank–Nicolson scheme. The pressure Poisson equation is solved by applying Fourier and cosine transforms along the spanwise and streamwise directions, and direct inversion in the wall-normal coordinate.

A graphical representation of the simulation set-up is given in figure 1. The computational domain starts at distance $\tilde{x}_0 = 33$ from the leading edge of the flat plate. This location defines the origin of the coordinate $x \equiv \tilde{x} - \tilde{x}_0$. Lengths are normalized by the inlet 99 % boundary-layer thickness, δ_0, and velocities are normalized by the free-stream value, U_∞. The inlet Reynolds number based on δ_0 is $Re_{\delta_0} = 800$ (in terms of the Blasius length scale, $\mathscr{L} = \sqrt{\tilde{x}\nu/U_\infty}$, the inlet Reynolds number is $Re_{\mathscr{L}_0} = 162$). In order to relate to the literature on fully turbulent flows, dimensionless wall distances $y^+ = yu_\tau/\nu$, forcing periods $T^+ = Tu_\tau^2/\nu$ and velocities $W^+ = W_0/u_\tau$ are supplied where beneficial. The friction velocity, u_τ, is extracted at the onset of the fully turbulent flow regime in the respective cases.

The length, width and height of the computational domain are 1200, 30 and 40, respectively, and the number of grid points in these dimensions are 4096, 192 and 192. The grid resolution is thus slightly finer than that adopted by Jacobs & Durbin (2001), who performed an extensive grid refinement study. The grid spacing in the streamwise (x) and spanwise (z) dimensions is uniform. Grid stretching using a hyperbolic tangent function is used in the wall-normal coordinate (y) to ensure a fine grid resolution near the wall. Throughout the streamwise extent of the computational domain, the coarsest grid resolution at the wall in terms of viscous units is $\Delta y^+_{wall} = 0.38$. The streamwise and spanwise grid spacings are $\Delta x^+ = 5.56$ and $\Delta z^+ = 2.95$, respectively.

The top boundary condition balances the growth of the boundary layer by a positive wall-normal velocity in order to ensure a zero mean pressure gradient in the streamwise direction. Homogeneous Neumann conditions are applied for the streamwise and spanwise velocity components at that boundary. A convective outflow condition is used at the exit of the domain, and periodicity is enforced in the spanwise direction. No-slip conditions are prescribed at the bottom wall. In addition, spanwise wall oscillation is applied over the full extent of the computational domain,

$$W(y = 0, t) = W_0 \cos\left(\frac{2\pi}{T} t\right). \tag{2.1}$$

The transverse forcing starts at the inlet of the computational domain, and causes the development of a Stokes boundary layer. It can be shown that, in the limit of large

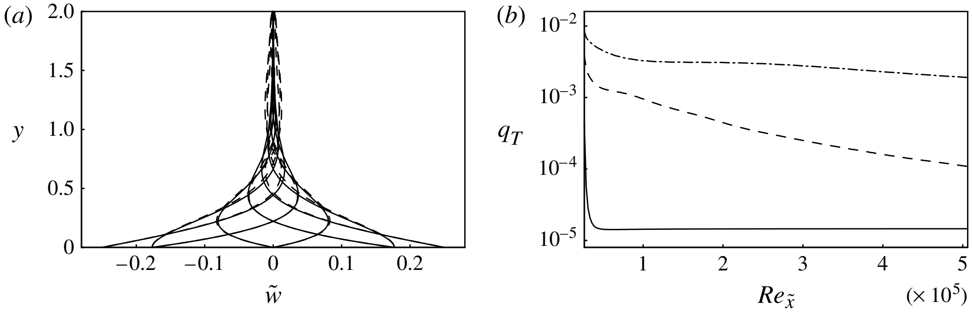

FIGURE 2. (a) Wall-normal profiles of $\tilde{w}(y, t)$ (solid) and W_{Stokes} (dashed) for $T = 200$. Eight equidistant phases are shown at $x = 200$. (b) Measure q_T for the deviation between $\tilde{w}(y, t)$ and W_{Stokes} as a function of downstream distance for $T = 10$ (solid), $T = 200$ (dashed) and $T = 800$ (dash-dotted).

downstream distances, the spanwise velocity field approaches the analytical solution to the Stokes second problem,

$$W_{Stokes}(y, t) = W_0 \exp\left(-\sqrt{\frac{\pi}{\nu T}}\,y\right)\cos\left(\frac{2\pi}{T}t - \sqrt{\frac{\pi}{\nu T}}\,y\right). \tag{2.2}$$

With increasing x, the thickness of the Stokes layer in the DNS, δ_w, becomes proportional to $\sqrt{2\pi T/\nu}$. The boundary-layer thickness, δ, on the other hand, grows with downstream distance. Therefore, beyond a small region near the inlet, the ratio δ_w/δ decays monotonically.

The time-harmonic forcing introduces a periodic component into the flow field. Hence a triple decomposition of flow variables is adopted,

$$a = \overbrace{\bar{a} + \tilde{a}_\varphi}^{\langle a\rangle_\varphi} \!\!\!\!\!\!\!\!\underbrace{\phantom{\tilde{a}_\varphi} + a'}_{a''}, \tag{2.3}$$

where $\bar{a}$ denotes the spanwise and time average, $\tilde{a}_\varphi$ is the periodic component and a' is the stochastic fluctuation. The quantity $\langle a\rangle_\varphi$ is the average at a particular phase, $\varphi(t) = (1/T)\,\mathrm{mod}(t, T)$, and comprises the time-averaged mean and the periodic component. The quantity a'' is the sum of the periodic component and the stochastic fluctuation.

For finite distances to the leading edge, the phase-averaged velocity profile $\tilde{w}(y, t)$ obtained from DNS differs from the analytical Stokes layer profile (2.2). This difference is presented in figure 2(a), and is quantified using the integral measure,

$$q_T(x) = \frac{1}{T\delta_w}\int_0^T\int_0^\infty \frac{\|\tilde{w} - W_{Stokes}\|}{W_0}\,\mathrm{d}y\mathrm{d}t. \tag{2.4}$$

The deviation of $\tilde{w}$ from the Stokes profile increases for longer oscillation periods, but remains at least two orders of magnitude smaller than $\tilde{w}$.

In order to initiate bypass transition in the simulations, the Blasius profile at the inlet to the computational domain is supplemented with a moderate level of free-stream turbulence with intensity $Tu_{FS} = 3\,\%$. Following Jacobs & Durbin

(2001), the inlet perturbations can be expressed as a weighted superposition of eigenfunctions of the continuous spectra of the homogeneous Orr–Sommerfeld and Squire operators. This approach inherently avoids the free-stream bias towards the streamwise component in the coupled Orr–Sommerfeld/Squire problem, which was recently pointed out by Dong & Wu (2013). Downstream of the inflow plane, the evolution of the flow is computed by direct simulations and therefore takes into account non-parallel and nonlinear effects. The methodology has been adopted successfully in a number of earlier studies (e.g. Brandt *et al.* 2004; Schrader, Brandt & Henningson 2009; Schrader, Subir & Brandt 2010). It faithfully reproduces the mechanics of bypass transition as demonstrated by a number of comparisons with experiments. For example, Brandt *et al.* (2004) and more recently Nolan & Zaki (2013) showed that the streamwise energy amplification and the downstream development of the shape factor agree with the results by Matsubara & Alfredsson (2001). The measurements by Mandal, Venkatakrishnan & Dey (2010) showed good agreement between the properties of their streaks and those observed by Jacobs & Durbin (2001). Matsubara & Alfredsson (2001) concluded that their results ‘provide an experimental verification of the simulated picture’.

The simulation set-up adopted herein excludes the leading-edge region. In two earlier studies, Nagarajan, Lele & Ferziger (2007) and later Ovchinnikov, Choudhari & Piomelli (2008) performed simulations of the entire plate including the leading edge. Their results showed that, when the leading edge is blunt or the free-stream turbulence intensity is relatively high, leading-edge receptivity can become important and should be taken into account. Their simulations also affirmed, however, that the approach adopted herein accurately captures the bypass transition mechanism that is active in the case of a slender leading edge.

The amplitudes of the individual inlet perturbations are assigned such that a von Kármán spectrum is obtained in the free stream,

$$E(\kappa) = Tu_{FS}^2 \frac{L^5\kappa^4}{C(1+(\kappa L)^2)^{17/6}}, \tag{2.5}$$

where Tu_{FS} is the free-stream turbulence intensity, and $\kappa = \sqrt{k_x^2 + k_y^2 + k_z^2}$ is the magnitude of the wavenumber vector. The length scale L is related to the integral scale $L_{11} = (1/Tu_{FS}) \int_0^\infty \overline{u'(x)u'(x+r)}\mathrm{d}r$ by $L = (55C/9\pi)L_{11}$. A choice of $C = 0.688$ leads to a peak of the energy spectrum at unit wavelength. The most energetic perturbations thus have wavelengths of the order of the boundary-layer thickness.

The downstream evolution of the perturbation field in the free stream is given in figure 3 for a reference simulation in the absence of wall oscillation. A nearly isotropic decay of the root mean square (r.m.s.) velocity fluctuations, which follows the power law $Tu_{FS} \sim \tilde{x}^{-0.69}$, is captured in figure 3(*a*). Figure 3(*b*) shows the integral length scale

$$L_k = \frac{k^{3/2}}{\varepsilon}, \tag{2.6}$$

where k is the turbulence kinetic energy and ε is the rate of energy dissipation, evaluated in the free stream and normalized by the local boundary-layer thickness. After an initial decay, the normalized length scale remains virtually constant over the remainder of the computational domain. A similar trend was observed in the experimental study by Kurian & Fransson (2009).

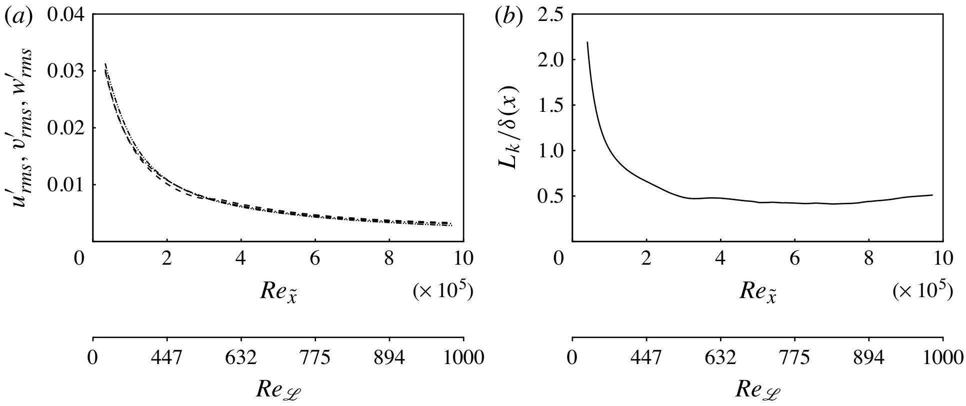

FIGURE 3. Free-stream decay of turbulence: (*a*) r.m.s. of the velocity fluctuations u' (dashed), v' (dash-dotted), w' (dash-double dotted) versus Reynolds number. (*b*) Turbulent length scale L_k normalized by the local boundary-layer thickness δ versus Reynolds number.

3. Integral performance measures

This section provides an overview of the effect of the wall oscillation on the transition process. Selected results obtained from the DNS are presented, and focus is placed on statistical measures that demonstrate the potential of the forcing to delay bypass breakdown.

The skin friction coefficient

$$C_f = \frac{\mu \left.\dfrac{\partial U}{\partial y}\right|_{y=0}}{\frac{1}{2}\rho U_\infty^2} \tag{3.1}$$

along the flat plate is reported in figure 4(*a*) for a range of forcing periods and a constant forcing amplitude, $W_0 = 0.25$. In agreement with the direct simulations by Jacobs & Durbin (2001), and the experimental studies of Roach & Brierley (1990), the maximum C_f at transition onset overshoots the turbulence correlation, $C_{f,\,turbulent} = 0.455 \ln^{-2}(0.06\, Re_{\tilde{x}})$ (White 2005). The downstream locations of the onset and completion of transition for all cases are identified by the first local minimum and the subsequent local maximum of the C_f curve, respectively. The corresponding Reynolds numbers, $Re_{\tilde{x},s}$ and $Re_{\tilde{x},e}$, are plotted in figure 4(*b*) versus the forcing period. For the reference case without forcing (given by $T = 0$), the transition process spans the Reynolds-number range $2 \times 10^5 \leqslant Re_{\tilde{x}} \leqslant 3.8 \times 10^5$, or $350 \leqslant Re_\theta \leqslant 650$, where θ is the momentum thickness.

The effect of the forcing on transition depends on the period of the spanwise flow. For the shortest period, $T = 10$, only a marginal deviation from the unforced reference case is observed, with transition completed at $Re_{\tilde{x}} \approx 4.3 \times 10^5$. In this context, it should be noted that the thickness of the Stokes layer scales as $\delta_w \sim \sqrt{T}$. Hence, for very short forcing periods, δ_w is small compared to the Blasius boundary-layer thickness, $\delta_w/\delta \ll 1$. In these cases, the spanwise flow is primarily limited to a region very close to the wall. For longer forcing periods, the thickness of the Stokes layer becomes larger, and has a more substantial influence on the transition process.

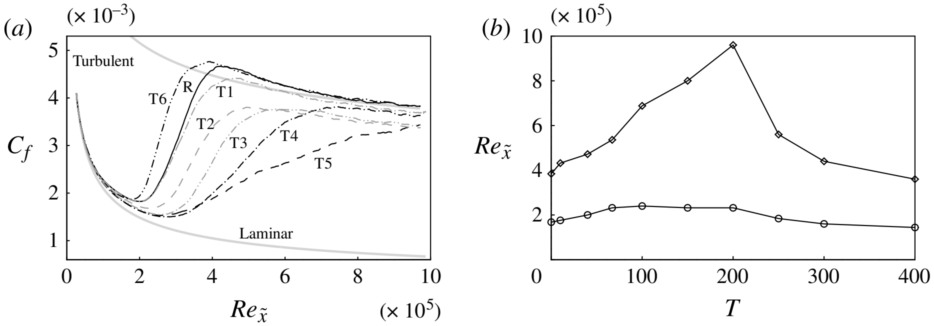

FIGURE 4. (*a*) Skin friction coefficient. Reference simulation (R, solid) and forcing with amplitude $W = 0.25$ and periods $T = 10$ (T1, grey dash-dotted), $T = 40$ (T2, grey dashed), $T = 67$ (T3, grey dash-double dotted), $T = 100$ (T4, black dash-dotted), $T = 200$ (T5, black dashed) and $T = 400$ (T6, black dash-double dotted). (*b*) Reynolds number at the onset ($Re_{\tilde{x},s}$, circles) and completion ($Re_{\tilde{x},e}$, diamonds) of transition.

Forcing with periods $T \in [40, 250]$ generally has two effects. The location of transition onset is shifted downstream. In addition, the transition region is extended in the streamwise direction. For the particular case $T = 200$, the flow is still intermittently laminar at the end of the simulation domain, which corresponds to $Re_{\tilde{x}} = 9.86 \times 10^5$. The remainder of this work focuses primarily on this particular case of 'optimal' forcing.

Any further increase of the forcing period beyond the optimal value quickly diminishes the delay in transition. The oscillation period $T = 300$ yields virtually identical values for transition onset and completion as the reference simulation. For $T = 400$, laminar–turbulent breakdown is accelerated and fully turbulent flow is established farther upstream than in the absence of spanwise forcing.

A wealth of earlier studies investigated the potential of spanwise wall oscillation to reduce drag in turbulent flows. The skin friction curves for the forcing periods of $T = 40$ and $T = 67$ reproduce this behaviour. After the completion of transition, the local wall shear in these cases remains between 10 and 12 % below the correlation for fully turbulent flow. In wall units, these forcing periods are $T^+ = 59$ and $T^+ = 99$, and the present forcing amplitude $W_0 = 0.25U_\infty$ is equivalent to $W^+ = 5.81$. Choi (2002) observed a reduction of drag in a turbulent boundary layer by approximately 45 % at $T^+ = 100$ and a higher amplitude $W^+ = 15$. For the same forcing period and a slightly lower amplitude $W_0^+ = 12$, Touber & Leschziner (2012) achieved a skin friction reduction by 38 % in fully turbulent channel flow. More recently, Lardeau & Leschziner (2013) found that the optimal forcing period of turbulent boundary layers is approximately $T^+ = 70$.

In order to determine whether transition delay yields an energetic advantage, the power requirement of the spanwise forcing, $\overline{P_{forcing}}$, must be taken into account. The net energetic gain is

$$\begin{aligned}\overline{P_{net}}(x) &= \overline{P_{prop,\,ref}}(x) - \overline{P_{prop,forced}}(x) - \overline{P_{forcing}}(x) \\ &= \Delta\overline{P_{prop}} - \overline{P_{forcing}},\end{aligned} \tag{3.2}$$

where $\overline{P_{prop,\,ref}}$ and $\overline{P_{prop,forced}}$ are the propulsion powers in the reference and forced cases. Results for $\overline{P_{net}}$ are provided in figure 5(*a*) for a range of forcing periods. Very

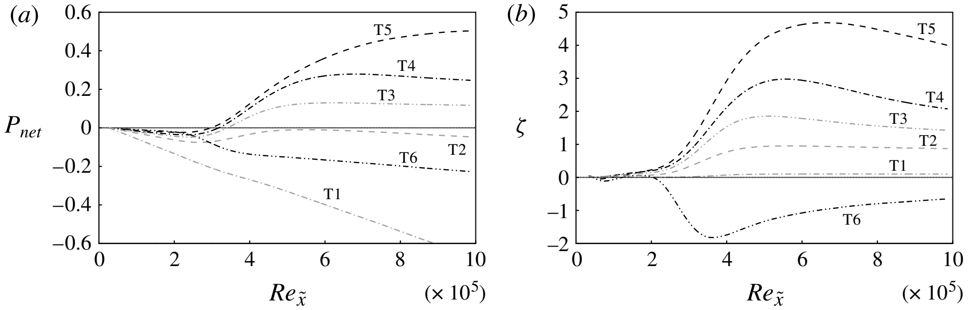

FIGURE 5. (*a*) Net savings. (*b*) Relative performance. Forcing with amplitude $W = 0.25$ and periods $T = 10$ (T1, grey dash-dotted), $T = 40$ (T2, grey dashed), $T = 67$ (T3, grey dash-double dotted), $T = 100$ (T4, black dash-dotted), $T = 200$ (T5, black dashed) and $T = 400$ (T6, black dash-double dotted).

short periods ($T = 10$) show the most negative energetic balance. This outcome is due to a negligible reduction of overall drag, combined with a relatively high power requirement, since $\overline{P_{forcing}} \sim 1/\sqrt{T}$. When the forcing period is increased, transition delay and a continuously decreasing power requirement of the forcing lead to an optimum $\overline{P_{net}}$ at $T = 200$. Beyond this forcing period, there is a sharp increase in overall drag and thus $\overline{P_{prop}}$, which outweighs the further decrease in the forcing power requirement. For $T = 400$, the acceleration of the breakdown process causes $\Delta\overline{P_{prop}}$ to become negative.

The relative energetic performance,

$$\zeta = \frac{\Delta\overline{P_{prop}}(x)}{\overline{P_{forcing}}(x)}, \tag{3.3}$$

normalizes the power savings by the power input into the spanwise forcing. Figure 5(*b*) presents ζ for a range of forcing periods and shows that the energetic savings at the optimal forcing period outweigh the power requirement of the transverse forcing by a factor of four.

The statistical results presented so far clearly demonstrate the ability of the wall forcing to reduce viscous drag, and motivate an examination of the underlying behaviour of the flow. A concise overview of the influence of the forcing on the transition process is provided by the space–time diagrams in figure 6. The contours represent the level of the streamwise velocity at a particular spanwise position for a long span of time. Dark regions correspond to fully turbulent flow. Each of the ‘wedges’ pointing upstream represents the formation of a single turbulent spot. It is seen that, in the presence of the forcing, the frequency of occurrence of breakdown events is markedly reduced.

In the subsequent sections, the cause of the change in transition location and the frequency of spot inception are examined. The influence of the optimal wall forcing on boundary-layer streaks is discussed, followed by a study of the secondary instability of the base flow.

4. Effect of optimal forcing on the pre-transitional boundary layer

Laminar boundary-layer streaks are a central element in bypass transition. Even though they are dominated by the streamwise velocity component, the streaks amplify

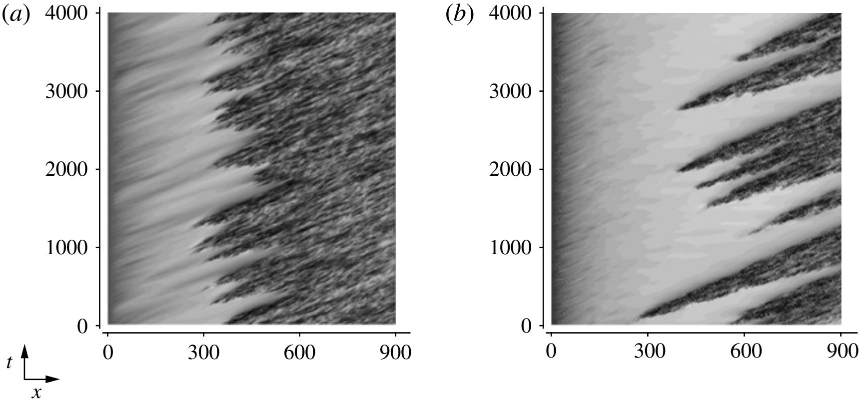

FIGURE 6. Space–time diagrams of the streamwise velocity, u, recorded at $y/\delta(x) = 0.40$. (*a*) Unforced reference case. (*b*) Optimal forcing.

due to a displacement of the mean momentum by relatively weaker wall-normal perturbations. This section presents a comprehensive analysis of the influence of the spanwise forcing on the streaks themselves, as well as on the lift-up mechanism that causes them.

4.1. *Boundary-layer streaks*

In the pre-transitional boundary layer, the streamwise stochastic fluctuations, u', provide a suitable starting point to examine the influence of the forcing on the streaks. Contours of the r.m.s. of u' are provided in figure 7. The reference case shows continuous growth of the fluctuation amplitude upstream of $Re_{\tilde{x},s}$, with the maximum located at $y/\delta(x) \approx 0.4$. This compares favourably with the experimental studies by Matsubara & Alfredsson (2001), who located the peak of the streamwise velocity fluctuation at 1.3 times the local displacement thickness, or equivalently $y/\delta(x) \approx 0.45$. A local peak is reached at the centre of the transition zone, $Re_{\tilde{x}} \approx 3 \times 10^5$. Once the flow has become fully turbulent, the position of the maximum u'_{rms} moves closer to the wall and is located at approximately 5 % of the local boundary-layer thickness. In the presence of the forcing (figure 7*b*), initial streak growth remains below the levels observed for the reference case. The results suggest that the amplification of streaks is delayed to larger $Re_{\tilde{x}}$.

The effect of the spanwise oscillatory flow on the streaks is also apparent in instantaneous flow fields. For the purpose of comparison, figures 8 and 9 show contours of u' from the reference and the optimal forcing simulations. The plane views are at constant $y/\delta(x)$, and thus follow the growth of the boundary layer. The top panel shows the free stream, where the perturbations decay as they are convected downstream in both cases. The three remaining panels are within the boundary layer.

Since they are generated by lift-up, the streaks close to the edge of the boundary layer are generally slower than the surrounding fluid, $u' < 0$. On the other hand, near-wall streaks ($y/\delta(x) = 0.20$) are characterized by a velocity surplus relative to the mean flow, $u' > 0$. Inside the boundary layer, the formation of streaks is significantly weakened by the spanwise oscillatory flow (figure 9). The influence of the forcing is most apparent at $y/\delta(x) = 0.20$, where $\tilde{w}$ is highest among the shown planes. The flow field in that view is free from Klebanoff streaks upstream

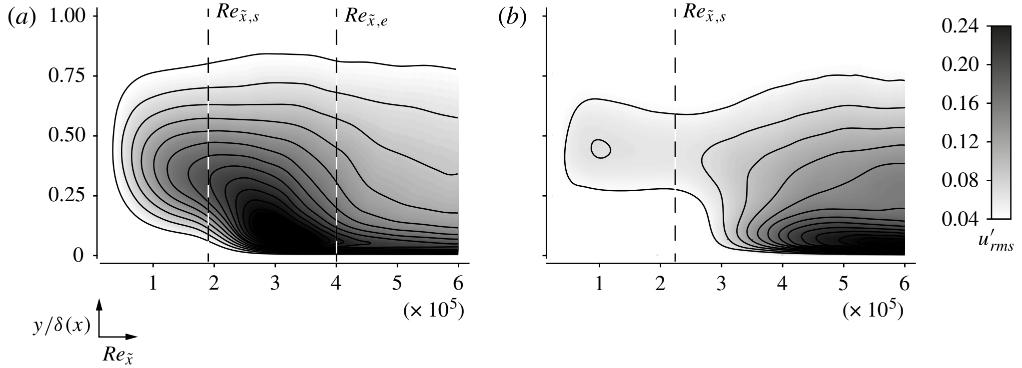

FIGURE 7. R.m.s. of the streamwise stochastic velocity fluctuations, $0.04 \leqslant u'_{rms} \leqslant 0.24$. (*a*) Reference simulation. (*b*) Optimal forcing.

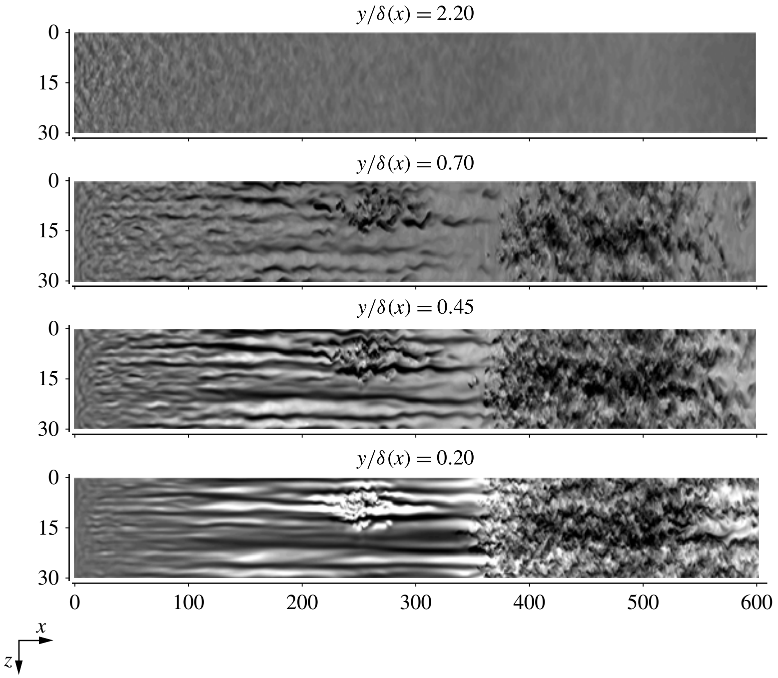

FIGURE 8. Top views, unforced reference simulation. Contours of the stochastic fluctuation of the streamwise velocity component $-0.20 \leqslant u' \leqslant 0.20$.

of $x \approx 350$. Relative to figure 8, the flow fields under the influence of the forcing clearly indicate an absence of energetic streaky structures in the boundary layer. Isolated streamwise-elongated features are observed, which are nonetheless shorter in extent than those in the reference case. The flow remains laminar, without any localized breakdown events, until a sudden change to fully turbulent flow near $x \approx 800$ ($Re_{\tilde{x}} = 6.67 \times 10^5$).

In order to examine the spectral content of the fluctuation field, the energy frequency spectrum is evaluated,

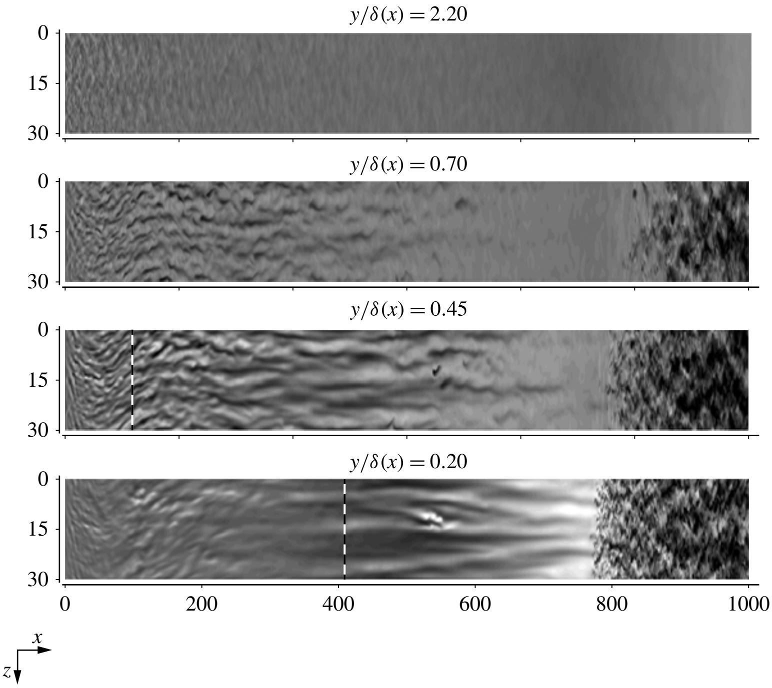

FIGURE 9. Top views, optimal forcing. Contours of the stochastic fluctuation of the streamwise velocity component, $-0.20 \leqslant u' \leqslant 0.20$. The dashed vertical line gives the location where the plane crosses the spanwise Stokes layer.

$$\hat{E}_u(F) = \left(\int_{-\infty}^{\infty} u'(t) \exp(-2\pi \mathrm{i} F t) \mathrm{d}t \right)^2, \tag{4.1}$$

where $F = 10^6 \omega \nu / U_\infty^2$ is the non-dimensional frequency. It should be noted that the lowest frequency at the inflow is $F = 480$, which is relatively high in comparison to that of the streaks. As demonstrated in earlier works, nonlinear interactions lead to the rapid broadening of the spectrum and the maximum shifts towards the low-frequency streamwise-elongated streaks (Jacobs & Durbin 2001; Brandt *et al.* 2004). The spectrum for the reference and forced cases at the downstream position $x = 170$ ($Re_{\tilde{x}} = 1.62 \times 10^5$), which is located upstream of spot inception, is given in figure 10. At this location, the local thickness of the spanwise Stokes layer is $\delta_w(x)/\delta(x) = 0.32$. The energy of the streamwise velocity component is primarily in the low-frequency range and decreases logarithmically with increasing frequency for both the reference and unforced cases. The presence of the forcing nonetheless reduces the energy contained in low-frequency perturbations by more than an order of magnitude. This finding affirms that the decrease in u'_{rms} can be attributed to the weakening of the streaks in the presence of spanwise wall oscillation.

Farther downstream, at $x = 400$, the flow in the reference simulation has become intermittent, and an increase of the energy in high-frequency perturbations is recorded in the spectra. A similar trend is observed for the forced case, although, in absolute terms, the energy level remains substantially below the reference case for all F. At this downstream position, the local thickness of the spanwise Stokes layer is $\delta_w(x)/\delta(x) = 0.21$.

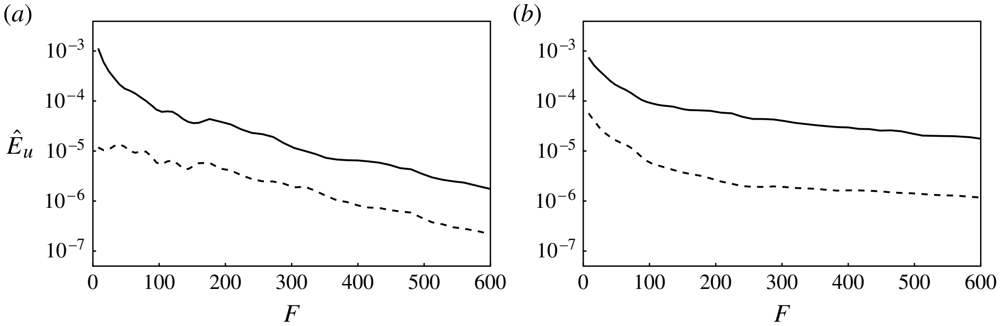

FIGURE 10. Temporal energy spectra of the streamwise velocity fluctuation u', evaluated at $y/\delta(x)=0.4$: (*a*) $x=170$; (*b*) $x=400$. Reference simulation (solid) and optimal forcing (dashed).

The spectral make-up of the disturbance field in terms of the spanwise perturbation wavenumber, k_z, is evaluated as

$$E_u(k_z, F) = \left(\int_{-\infty}^{\infty} \int_{-\infty}^{\infty} u'(z, t) \exp(-\mathrm{i}2\pi(Ft + k_z z)) \mathrm{d}t \mathrm{d}z \right)^2 . \qquad (4.2)$$

Results for the reference and optimally forced cases are compared in figure 11. The spectra show small energy content at low Reynolds number owing to the absence of low-frequency disturbances at the inlet. Downstream of that region, the reference simulation develops highly energetic perturbations, with a peak at spanwise wavenumber $k_z \approx 1.4$. The corresponding spanwise wavelength is approximately twice the local boundary-layer thicknesses, which is representative of the pre-transitional streaks. Transition to turbulence downstream of $Re_{\tilde{x}} \approx 2 \times 10^5$ is characterized by a redistribution of energy, which causes $E_u(k_z, F=16)$ to decay. In the presence of the wall motion, the initial amplification of low-frequency perturbations is substantially reduced. The level of E_u remains below that of the reference case throughout the investigated range of Reynolds numbers.

4.2. *Lift-up mechanism*

In order to examine the mechanism for the weakening of the streaks, the budget of the kinetic energy in the streamwise velocity fluctuation, $k^u = \frac{1}{2}\overline{u'u'}$, is considered,

$$\underbrace{\overline{u_l} \frac{\partial}{\partial x_l} k^u}_{C^u} + \underbrace{\overline{u'u'_l} \frac{\partial}{\partial x_l} \overline{u}}_{P^u} = \underbrace{-\frac{1}{\rho} \frac{\partial}{\partial x} \overline{u'p'}}_{R^u} \underbrace{- \nu \overline{\frac{\partial}{\partial x_l} u' \frac{\partial}{\partial x_l} u'}}_{D^u} \underbrace{- \frac{1}{2} \frac{\partial}{\partial x_l} \overline{u'_l u' u'}}_{T^u} + \nu \frac{\partial^2}{\partial x_l \partial x_l} k^u . \qquad (4.3)$$

The terms in this equation describe the advection (C^u), production (P^u), pressure redistribution (R^u), dissipation (D^u) and turbulent transport (T^u) of disturbance kinetic energy. Since k^u is dominated by the streaks, the production term, P^u, is directly related to amplification of streaks via the lift-up process. The boundary layer integrals of the production, dissipation, convection and pressure reduction terms of k^u for both the reference and optimally forced cases are presented in figure 12. A significant reduction in P^u is observed in the presence of the wall motion, where the streaks are

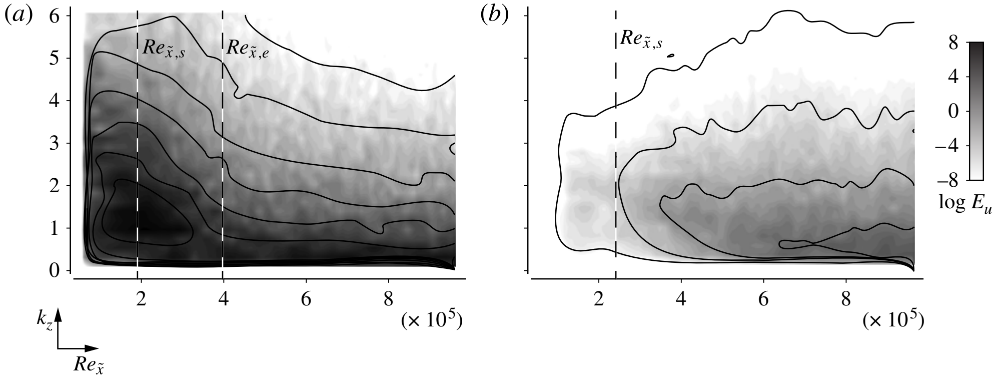

FIGURE 11. Logarithm of the spanwise energy spectra of u' versus downstream Reynolds number at $y/\delta(x) = 0.40$. (*a*) Reference simulation. (*b*) Optimal forcing. The contours span the range $-8 \leqslant \log E_u \leqslant 8$, for $F = 16$.

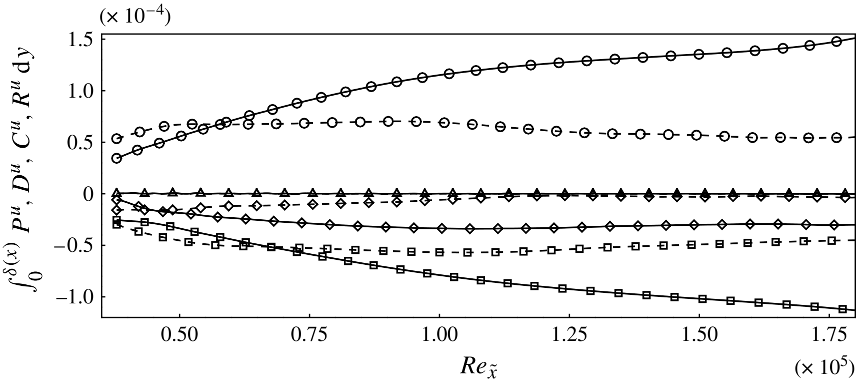

FIGURE 12. Budget of the kinetic energy in streamwise stochastic fluctuations, integrated over the local thickness of the boundary layer. Production (P^u, circles), dissipation (D^u, squares), convection (C^u, diamonds) and pressure redistribution (R^u, triangles). Reference (solid) and forced (dashed) cases.

also weaker. Outside a small region near the inflow, the dissipation of kinetic energy is also significantly lower in the forced case.

In order to further assess the influence of the wall forcing on the lift-up mechanism, the joint probability density function (PDF) of u' and v', or $G(u', v')$, is evaluated. The probability P for a pair of values (u', v') to lie within the interval $[u'_1, u'_2] \times [v'_1, v'_2]$ is obtained by integrating $G(u', v')$,

$$P([u'_1, u'_2] \times [v'_1, v'_2]) = \int_{v'_1}^{v'_2} \int_{u'_1}^{u'_2} G(u', v') \mathrm{d}u' \mathrm{d}v'. \tag{4.4}$$

The free-stream behaviour of the fluctuation field at the wall distance $y/\delta(x) = 1.6$ is given in figure 13(*a*). The circular contours reflect the isotropy of the free-stream perturbation field. Inside the boundary layer, the shape of the contour lines is stretched in the u' direction and compressed in the v' direction. The reduced extent

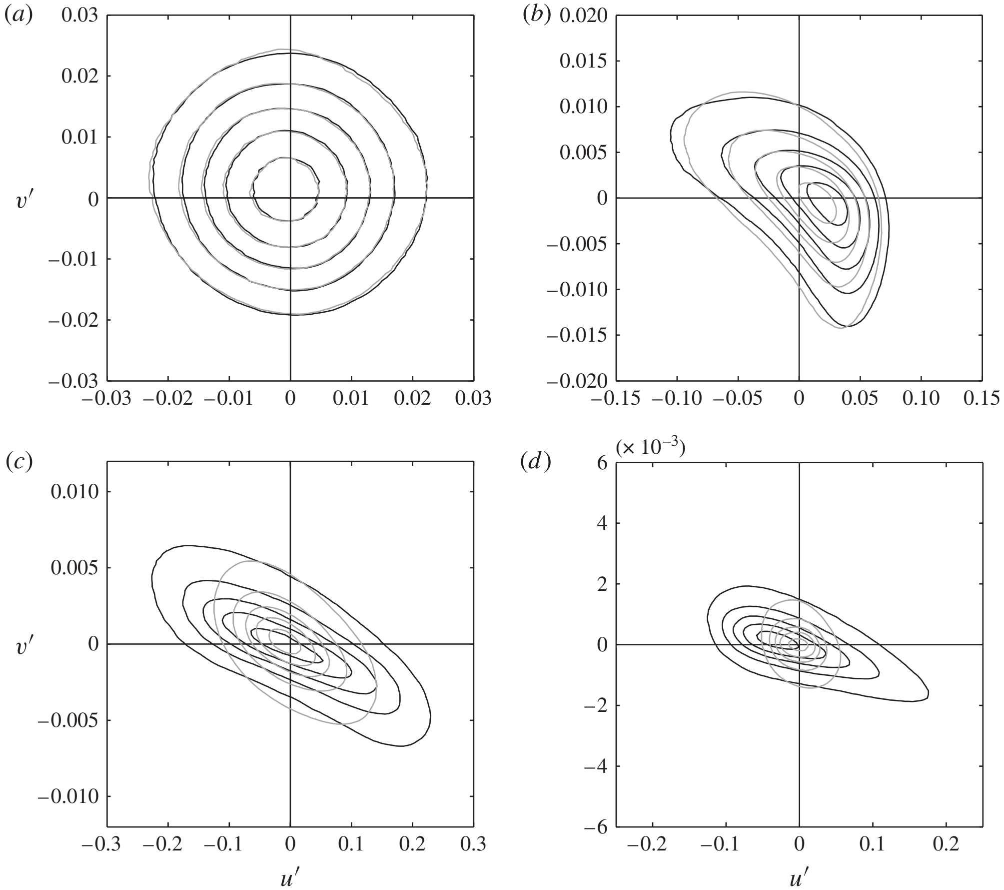

FIGURE 13. Joint PDFs for the streamwise and wall-normal velocity fluctuations at $x = 170$: (*a*) $y/\delta(x) = 1.6$; (*b*) $y/\delta(x) = 0.8$; (*c*) $y/\delta = 0.4$; (*d*) $y/\delta = 0.2$ (located inside the spanwise Stokes layer). Contours give lines of 10, 30, 50, 70 and 90 % probability for the reference simulation (black) and optimal forcing (grey).

of the joint PDFs with respect to v' can be attributed to the combined effects of shear sheltering and wall blocking. The formation of Klebanoff streaks within the boundary layer causes the expansion of the joint PDFs in the direction of u'. In the reference case, the joint PDFs become increasingly biased towards quadrants II (ejections: $u' < 0,\ v' > 0$) and IV (sweeps: $u' > 0,\ v' < 0$) inside the boundary layer. Both sweeps and ejections are markedly weakened in the presence of the forcing. This effect is most noticeable close to the wall, where the magnitude of the spanwise base flow is highest.

In order to examine whether there exists a preferential orientation in spectral space for energy amplification, the quantity

$$\varepsilon_u = \int_0^{\delta(x)} \log E_{u,forced} - \log E_{u,\,ref} \mathrm{d}y \tag{4.5}$$

is considered. Here, E is the kinetic energy as a function of F and k_z. The results for the streamwise and wall-normal fluctuations, respectively, are shown in figure 14(*a*,*b*).

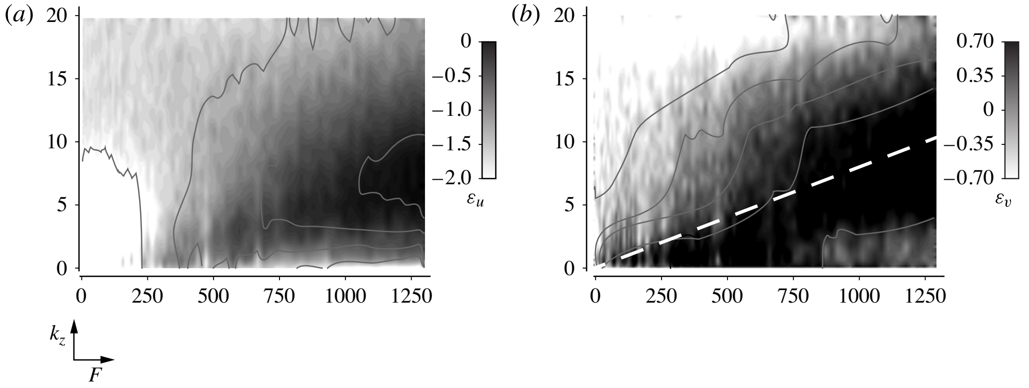

FIGURE 14. Difference between the energy of reference and optimally forced cases at $x = 65$, integrated over the extent of the boundary layer. (*a*) Streamwise component $-2 \leqslant \varepsilon_u \leqslant 0$. (*b*) Wall-normal component $-0.7 \leqslant \varepsilon_v \leqslant 0.7$.

When considering u', it should be emphasized that ε_u is negative for all F and k_z. The difference is most pronounced in the region $F < 200$, $k_z < 10$, which is associated with boundary-layer streaks.

The difference in the spectra of v', on the other hand, contains regions of both positive and negative ε_v. The energy in the forced case is highest along rays starting at the origin, and pointing towards $F = 1300$, $k_z = 10$, marked by the dashed line in figure 14(*b*). The non-dimensional frequency is related to the streamwise wavenumber of the perturbations via $k_x = FU_\infty^2/(10^6 c\nu)$, where c is the phase speed of the disturbance. Assuming $c \in [0.4, 0.85]$, the angle of these rays ranges from 14 to 6°. This angle has been explained using a model problem and comparing the diffusive and convective time scales of free-stream perturbations (Hack & Zaki 2012). Owing to the wall forcing, the base flow is three-dimensional. Disturbances whose wavenumber vector is perpendicular to the shear vector can preferentially diffuse into the boundary layer.

4.3. *Streak amplitudes*

The discussion of the amplitude of boundary-layer streaks has thus far relied on statistical measures of u'. For example, it was shown that the r.m.s. of u' decreases under the influence of the spanwise wall forcing. These results do not, however, differentiate the part of u' that indeed forms the streaks from the surrounding perturbations, since the entire disturbance field is sampled indiscriminately. In order to identify particular streaks, the methodology described by Nolan & Zaki (2013) is applied to time series that comprise 4000 snapshots from each of the reference and the optimally forced cases.

First, laminar flow regions are isolated using a laminar–turbulent discrimination technique. The local extrema of u' are subsequently identified in cross-flow planes, and streaks are reconstructed by connecting the extrema across adjacent planes. Using this approach, the streaks can be identified (see figure 15) and traced in space–time as Lagrangian objects. The spatial coordinates of streak s are given by $\boldsymbol{x}^s(t)$, and its amplitude is $\mathscr{A}_u^s(\boldsymbol{x}^s, t) \equiv u'(\boldsymbol{x} = \boldsymbol{x}^s, t)$.

The average of the amplitudes of all streaks, $\overline{\mathscr{A}_u} = (1/S) \sum_s \mathscr{A}_u^s$, is shown in figure 16 as a function of the downstream coordinate. Generally, the amplitudes of

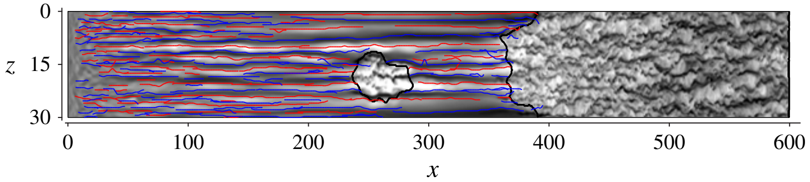

FIGURE 15. High-speed (red) and low-speed (blue) streaks are identified in a flow field from the reference simulation. Black lines demarcate regions of turbulence. The background contours represent the streamwise velocity fluctuations, $-0.30 \leqslant u' \leqslant 0.30$.

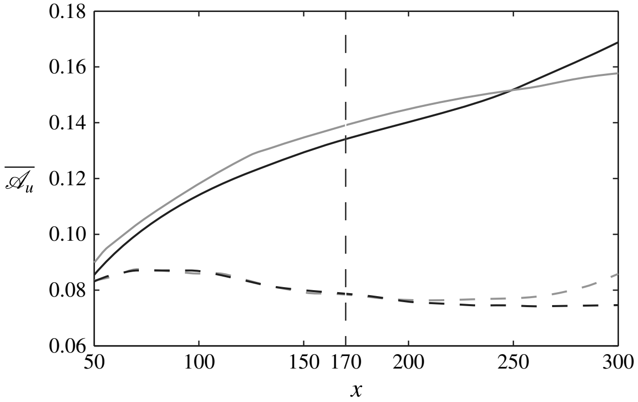

FIGURE 16. Amplitudes of high-speed (black) and low-speed (grey) streaks for reference (solid) and optimally forced (dashed) cases versus downstream position.

high-speed and low-speed streaks are approximately equal, in both the reference and forced cases. For the former, an increase in the amplitude with x is observed, and $\overline{\mathscr{A}_u}$ grows from 0.09 at $x = 50$ to 0.16 at $x = 300$. In the presence of the spanwise flow, the averaged amplitudes are significantly lower, and the relative difference to the reference simulation grows with downstream distance. At $x = 300$, the forcing has caused a reduction in the streak amplitude by a factor of two.

The PDFs of $\mathscr{A}_u^s$ for both the reference and forced cases at $x = 170$ are presented in figure 17. Solid lines mark a fit for a type I general extreme value distribution. Inspection of the reference simulation shows that the peak of the PDF is located at approximately 15 % of the free-stream velocity for both high- and low-speed streaks. The wall forcing, on the other hand, leads to substantially narrower PDFs, with amplitudes of the majority of the streaks below 10 % of the free-stream velocity. It also eliminates high-amplitude streaks, $\mathscr{A}_u^s > 0.25$. Further analysis of the effect of the wall motion on the streaks is presented in figure 18, where the phase-averaged amplitude, $\langle \mathscr{A}_u \rangle$, is plotted versus the phase of the base flow at $x = 170$. In the forced case, the streak amplitude oscillates twice per base-flow period between $\langle \mathscr{A}_u \rangle = 0.07$ and 0.10. This frequency doubling is expected since the wall oscillation is symmetric in the positive and negative spanwise directions. Despite this preferential amplification at $\varphi \approx 0.15$ and $\varphi \approx 0.65$, the streak amplitudes remain significantly weaker in the presence of the forcing relative to the reference simulation.

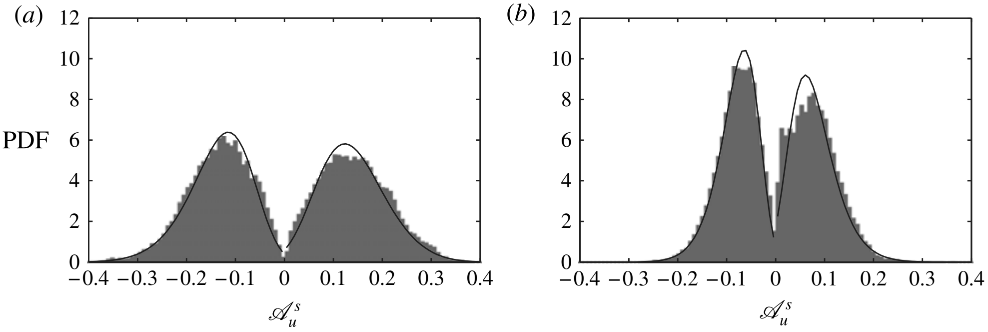

FIGURE 17. PDFs of the local streak amplitudes at $x = 170$. (*a*) Unforced reference case. (*b*) Optimal forcing.

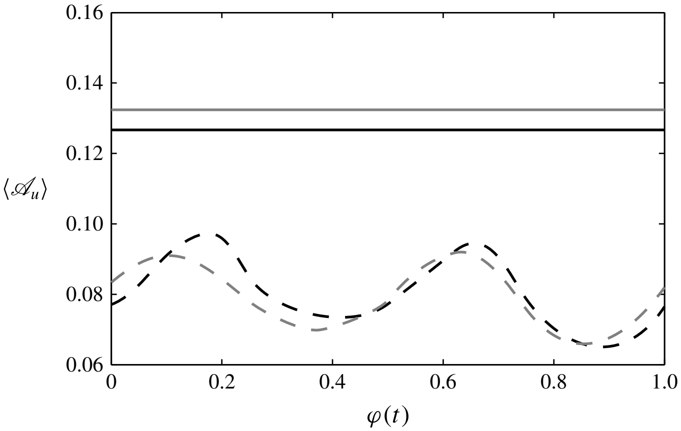

FIGURE 18. Amplitudes of high-speed (black) and low-speed (grey) streaks for reference (solid) and optimally forced (dashed) cases versus the phase of the base flow at $x = 170$.

Boundary-layer streaks initiate breakdown to turbulence via the amplification of secondary instabilities. The recent study by Hack & Zaki (2014) established a clear correlation between the amplitudes of streaks and the amplification rates of these instabilities. In that work, it was shown that the mean amplitude of the subset of streaks that cause breakdown to turbulence is approximately 30 % of the free-stream speed. This level of streak amplitude is nearly absent in the forced case. It is therefore expected that these streaks will be less likely to develop secondary instabilities – a point that is examined in detail in the next section.

5. Secondary instability and breakdown

The results presented so far have shown a substantial weakening of the boundary-layer streaks at the optimal wall oscillation. The low-frequency streaks themselves, however, do not immediately cause the formation of turbulent spots. Breakdown to turbulence is rather a consequence of high-frequency secondary instabilities of the streaky base state. The purpose of the present section is to relate the weaker boundary-layer streaks in the forced flow to the reduced frequency of turbulent-spot inception via the analysis of secondary instabilities.

5.1. *Secondary instability analysis*

The computational approach to investigate the secondary instability of the streaky boundary layer is based on the work of Blackburn & Sherwin (2004) and Barkley, Blackburn & Sherwin (2008). The base flow of the stability analysis is given by instantaneous velocity profiles in the cross-flow plane that are extracted from DNS fields. The dependence of the base flow on x and t is therefore parametric. This approach is motivated by the weak time dependence of the streaky base state. For the present case with optimal forcing ($T=200$), the time scale of the wall motion substantially exceeds that of the streak instabilities. The locally parallel base state of the instability analysis is $\boldsymbol{Q}_{stab}(y, z; x, t) = (U, V, W, P)^{\mathrm{T}}_{stab} = (u(x, y, z, t)_{DNS}, 0, 0, 0)^{\mathrm{T}}$. The secondary instability is described by the state vector $\boldsymbol{q}_2(x, y, z, t) = (u, v, w, p)^{\mathrm{T}}_2$, which leads to the ansatz $\boldsymbol{q} = \boldsymbol{Q}_{stab} + \boldsymbol{q}_2$ for the perturbed base state.

A normal-mode assumption is adopted in x,

$$\boldsymbol{q}_2(x, y, z, t) = \hat{\boldsymbol{q}}_2(y, z, t)\exp(\mathrm{i}\alpha x), \tag{5.1}$$

where α is the streamwise instability wavenumber. The streak instability is assumed to be small in magnitude, so that quadratic terms may be neglected. The time evolution of $\boldsymbol{u}_2 = (u, v, w)^{\mathrm{T}}_2$ is hence described by the linear relation

$$\frac{\partial}{\partial t}\hat{\boldsymbol{u}}_2 = -\mathrm{i}\boldsymbol{L}\hat{\boldsymbol{u}}_2, \tag{5.2}$$

where

$$\boldsymbol{L} = \mathrm{i}[(\boldsymbol{I} - \nabla\boldsymbol{\Delta}^{-1}\nabla\,\boldsymbol{\cdot}\,)(\boldsymbol{U}_{stab}\boldsymbol{\cdot}\nabla) + (\nabla\boldsymbol{U}_{stab})\,\boldsymbol{\cdot}\,] + \frac{1}{Re}\nabla^2, \tag{5.3}$$

and $\boldsymbol{\Delta}^{-1}$ is the formal inverse of the Laplacian. Integration of (5.2) gives

$$\hat{\boldsymbol{u}}_2(t) = \boldsymbol{A}(t)\hat{\boldsymbol{u}}_2(0), \tag{5.4}$$

with the fundamental solution operator $\boldsymbol{A} = \exp(-\mathrm{i}\boldsymbol{L}t)$. The time dependence of an eigenfunction $\hat{\boldsymbol{u}}_2$ of $\boldsymbol{L}$ with corresponding eigenvalue σ is hence given by $\hat{\boldsymbol{u}}_2(t) = \hat{\boldsymbol{u}}_2(0)\exp(-\mathrm{i}\sigma t)$. The investigated base flow is exponentially stable if the imaginary part σ_i of all eigenvalues is negative, and unstable otherwise. The numerical method for computing a subspectrum of $\boldsymbol{L}$ is based on the IRAM scheme introduced by Sorensen (1992). The boundary conditions for the secondary instability at the wall and at the top of the computational domain are

$$u_2, v_2, w_2 = 0 \qquad \text{for } y = 0, \tag{5.5}$$

$$v_2, \frac{\partial u_2}{\partial y}, \frac{\partial w_2}{\partial y} = 0 \qquad \text{for } y \to \infty. \tag{5.6}$$

Consistent with the DNS flow field, periodicity is enforced in the spanwise dimension.

A visualization of a representative eigenfunction of a secondary streak instability is provided in figure 19. Background contours show the streamwise fluctuation field and lines indicate the eigenfunction of the most unstable secondary instability. The top panel shows the entire spanwise extent of the computational domain and demonstrates that the eigenfunction is localized around a single low-speed streak. The two lower panels provide enlarged views of the streamwise and spanwise components of the instability eigenfunction. In the case of the streamwise component, the eigenfunction

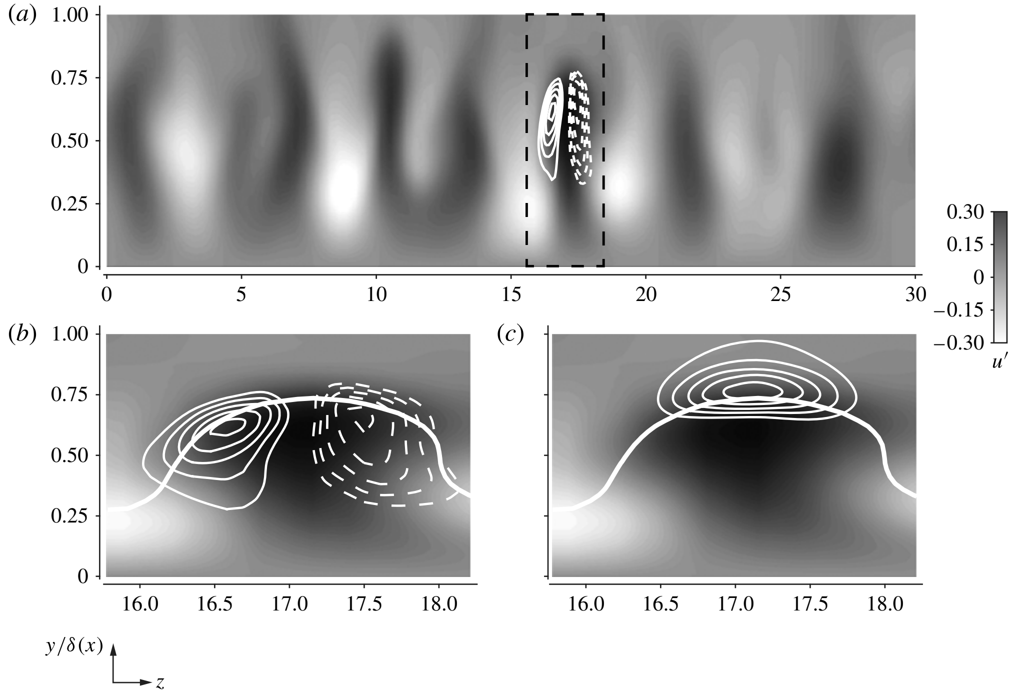

FIGURE 19. Eigenfunction of a streak instability (lines) and streamwise velocity fluctuation field $-0.30 \leqslant u' \leqslant 0.30$ (greyscale contours). (*a*) Entire spanwise extent of the domain with streamwise component of the eigenfunction. (*b*) Enlarged view with streamwise component of the eigenfunction. (*c*) Enlarged view with spanwise component of the eigenfunction. Dashed lines are negative values, and solid lines are positive values. The thick white line marks the critical layer.

is situated along the flanks of the streak and shows a spanwise antisymmetric configuration, such that u_2 is positive on the right-hand side and negative on the left-hand side of the streak. The eigenfunction of the spanwise component is situated on top of the streak and is spanwise symmetric with respect to the host streak. The combined effect of the two components is a sinusoidal deformation of the host streak, which grows in amplitude and eventually leads to the inception of a turbulent spot.

In order to examine the impact of the wall forcing on the amplification of secondary instabilities, a statistical approach using a large number of stability analyses is pursued. The time interval between two consecutive analyses is $\Delta t_{stab} = 20$. This time interval ensures that different phases of the oscillatory base flow are examined. A total of 200 time instances were investigated at the downstream position $x = 170$. It should be noted that the streamwise wavenumber α is an input parameter of the linear analysis. Therefore, at each time instance, six stability computations over the range $\alpha \in [0.3, 1.3]$ were performed. This choice is motivated by earlier studies (Hack & Zaki 2014), which examined the range of α in detail. Only the maximum growth rate is included in the reported statistics. Furthermore, it should be pointed out that the instability analysis is purely temporal and thus differs from the DNS, which captures the spatio-temporal evolution of the instabilities. In a recent study, however, Hack & Zaki (2014) have demonstrated that the temporal analysis can accurately capture the properties of the secondary instabilities of streaks.

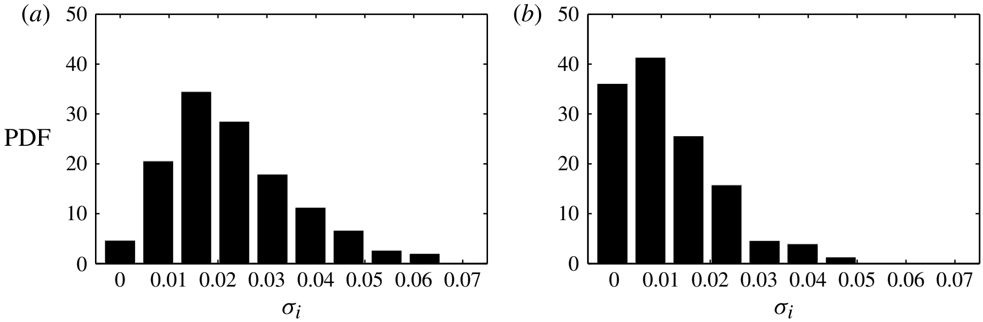

FIGURE 20. PDFs of the growth rate σ_i of the streak instabilities, evaluated at $x = 170$. (a) Unforced reference case. (b) Optimal forcing.

The results from the current stability analyses are presented in figure 20. The mean growth rate of the secondary instabilities halves from $\overline{\sigma_{i,\,ref}} = 0.023$ in the reference case to $\overline{\sigma_{i,forced}} = 0.011$ under the influence of the wall forcing. This reduction affects all growth rates in excess of 0.02. The work by Hack & Zaki (2014) demonstrated that secondary instabilities with higher growth rates can be directly related to breakdown via turbulent spots. The current analysis thus explains the reduced frequency of occurrence of turbulent spots in the presence of the spanwise wall forcing, which was shown in the space–time diagram (figure 6).

5.2. *Formation of turbulent spots*

For a closer study of the influence of the wall motion on the formation of turbulent spots, the space–time diagram from figure 6 is repeated in figure 21 for a longer time interval, $t \in [0, 8000]$. Comparison of the reference and forced cases substantiates the earlier observation of a lower rate of spot formation in the forced flow. In order to quantitatively corroborate the visual impression from the figure, the laminar–turbulent discrimination technique is employed, and the inception of turbulent spots is recorded. PDFs of the downstream position of spot inception are shown in the two lower panels of figure 21. It is seen that in the reference case practically all spots form upstream of $x \approx 400$. In the presence of the forcing, the average location of spot formation is shifted downstream, with the peak of the distribution located at $x \approx 800$.

The laminar–turbulent discrimination method may also be used to determine the fraction of time for which the flow at a given downstream location is turbulent. The indicator function $\varGamma(x, y, z, t)$ is set to unity if the flow is turbulent and to zero if the flow is laminar. Intermittency is then defined as the time and spanwise average of $\varGamma$,

$$\gamma(x, y) = \lim_{t^* \to \infty} \frac{1}{t^* L_z} \int_{t^*} \int_{L_z} \varGamma(x, y, z, t)\mathrm{d}z\mathrm{d}t, \tag{5.7}$$

and the local peak intermittency is

$$\gamma_p(x) = \max_y \gamma(x, y). \tag{5.8}$$

Figure 21 shows that the flow in the reference simulation becomes fully turbulent at $x \approx 600$ ($Re_{\tilde{x}} = 5.06 \times 10^5$). In the presence of the forcing, the flow approaches $\gamma_p = 1$ at the downstream end of the computational domain, at $x = 1200$ ($Re_{\tilde{x}} = 9.86 \times 10^5$). The delay in breakdown to turbulence has been attributed to the weaker streaks in the pre-transitional flow and their reduced secondary instability.

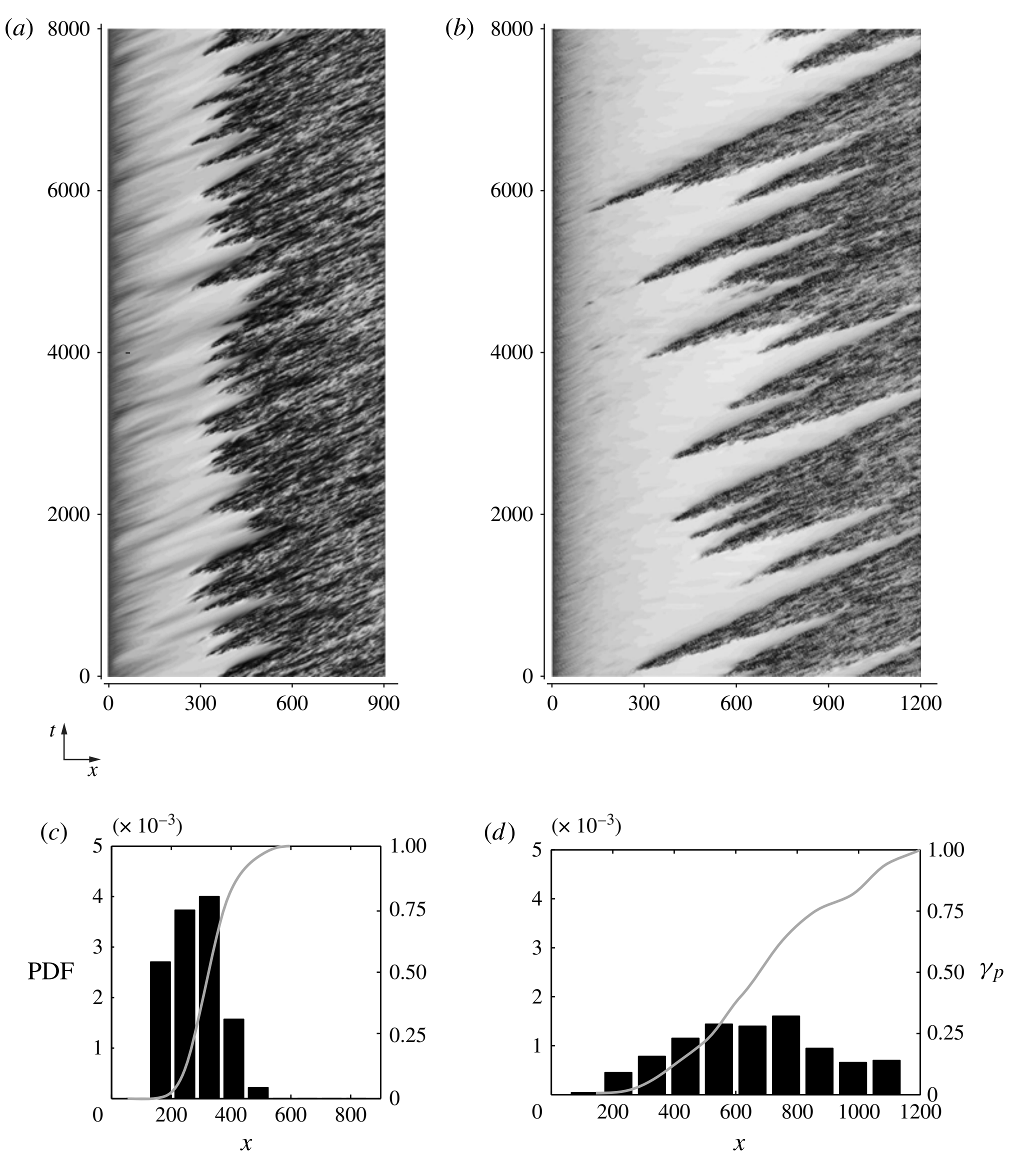

FIGURE 21. (*a*,*b*) Space–time diagrams of the streamwise velocity, u, at $y/\delta(x) = 0.40$. (*c*,*d*) PDFs of the location of spot inception. The grey line gives the local peak intermittency γ_p. (*a*,*c*) Unforced reference case. (*b*,*d*) Optimal forcing.

6. Discussion

6.1. *Variation of the forcing amplitude*

The wall forcing is characterized by its period, T, and its amplitude, W_0. While the influence of T was comprehensively examined in § 3, the forcing amplitude has so far been kept constant at $W_0 = 0.25$. In order to provide a qualitative understanding of the influence of the forcing amplitude on the transition process, additional simulations were performed at various W_0. For the two forcing periods $T = \{40, 200\}$, two

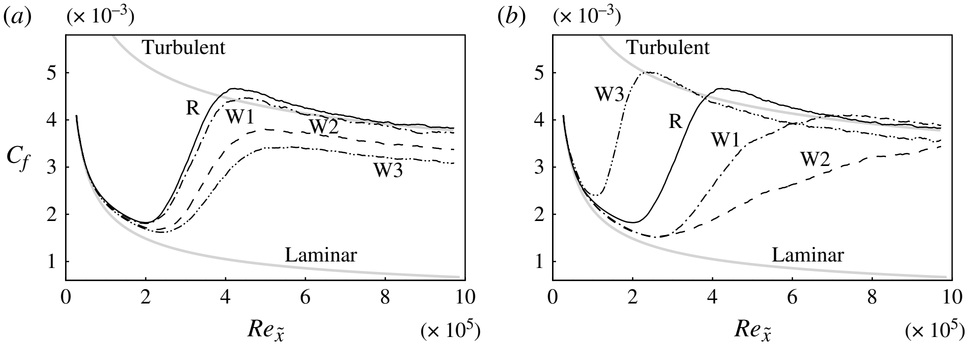

FIGURE 22. Skin friction coefficient under variation of the forcing amplitude: (*a*) $T = 40$; (*b*) $T = 200$. Reference simulation (R, solid), $W_0 = 0.10$ (W1, dash-dotted), $W_0 = 0.25$ (W2, dashed) and $W_0 = 0.40$ (W3, dash-double dotted).

additional amplitudes $W_0 = 0.10$ and $W_0 = 0.40$ were examined. All other parameters, including the turbulent inlet condition and the grid resolution, remained unchanged.

Further study of the period $T = 40$ is motivated by the earlier reported reduction of skin friction in fully turbulent boundary layers at similar forcing periods (e.g. Lardeau & Leschziner 2013). The skin friction coefficient is shown in figure 22(*a*). Both the onset and the completion of the transition process are increasingly shifted downstream with growing forcing amplitude. After the completion of transition, the local skin friction remains below the characteristic level of fully turbulent flow. This effect is more pronounced for higher forcing amplitudes, and thus qualitatively matches the results in various studies of viscous drag reduction in turbulent bounded shear flows.

A second series of computations was performed for $T = 200$. This particular oscillation period was the optimal configuration with respect to transition delay and reduction in viscous drag at $W_0 = 0.25$. The local skin friction coefficient is shown in figure 22(*b*), and demonstrates a strong dependence of the transition process on the amplitude of the forcing. For $W_0 = 0.10$, the onset of transition is at the same downstream position as for $W_0 = 0.25$, yet the streamwise extent of the transition region itself is substantially shortened. An increase in the forcing amplitude to $W_0 = 0.40$ sharply reverses the stabilizing effect of the forcing, and a very rapid breakdown to turbulence is observed, with transition starting upstream of the unforced case, at $x \approx 100$. Fully turbulent flow is observed as early as $x \approx 300$.

The fluctuation field in the case $T = 200$, $W_0 = 0.40$ shows a clear phase dependence as demonstrated by the phase-averaged space–time diagrams provided in figure 23. Contours show the spanwise standard deviation of the fluctuation field,

$$\langle u' \rangle_{rms} = \left(\frac{1}{NL_z} \sum_N \int_0^{L_z} u'^2 \mathrm{d}z \right)^{1/2}, \tag{6.1}$$

where $N = 20$ is the number of sampled periods of the base flow. The periodicity is most prominent at the considered wall distance, $y/\delta(x) = 0.30$, which is slightly lower than the location of the peak u' associated with Klebanoff streaks.

Results for the streamwise velocity component are shown in figure 23(*a*). A structure of alternating bands of high and low $\langle u' \rangle_{rms}$ is observed with half the period of the base flow. In other words, each forcing period contains two intervals during

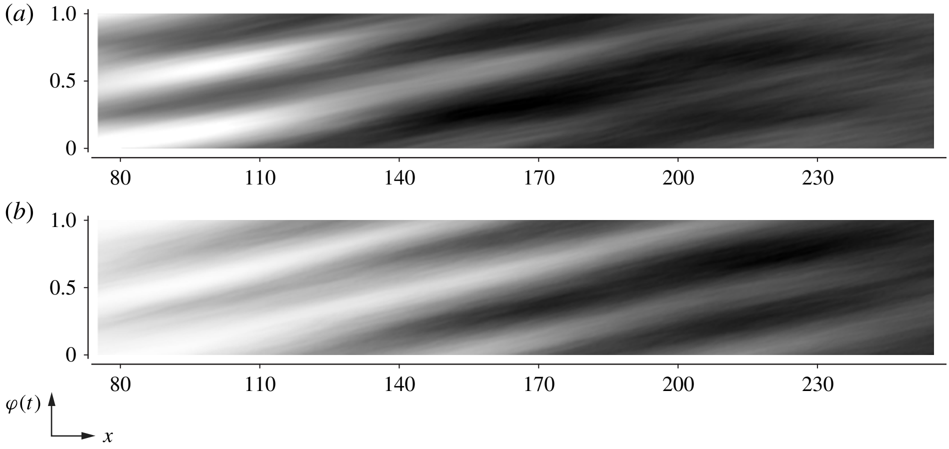

FIGURE 23. Phase-averaged space–time diagrams: (*a*) $\langle u' \rangle_{rms}$; (*b*) $\langle v' \rangle_{rms}$. Forcing with $T = 200,\ W_0 = 0.40$.

which the fluctuations grow, separated by intervals in which the fluctuations decay again. The bands are aligned at an angle to the abscissa, which corresponds to a characteristic 'speed' $c_c \approx 0.60$ with which the perturbation field travels downstream. As the flow becomes increasingly turbulent, the bands smear out and finally form a continuous region of high $\langle u' \rangle_{rms}$.

The standard deviation of the wall-normal velocity fluctuation, v', shows a very similar behaviour (figure 23*b*). While the magnitude of $\langle v' \rangle_{rms}$ is initially lower than for the streamwise component, the observed angle of the bands is approximately identical. It is also clear that the phases of the streamwise and wall-normal fluctuations match, indicating a simultaneous amplification and decay of the two components.

Making use of the methodology introduced in § 5.2, spot formation in the case $T = 200$, $W_0 = 0.40$ is investigated. Figure 24(*a*) shows a probability distribution for the formation of turbulent spots as a function of the phase of the base flow, irrespective of the downstream position at which breakdown occurs. Two mildly pronounced peaks are observed, which indicates that the frequency of breakdown to turbulence is the first harmonic of the base flow frequency. This phase dependence becomes more evident if the downstream position of the turbulent spots is incorporated to compute a corrected phase of spot inception using the phase speed $c_c = 0.60$. In figure 24(*b*), two well-defined maxima are seen, indicating a strong phase dependence of breakdown to turbulence in the case of high-amplitude forcing. Top views of the flow field for this case, $T = 200$ and $W_0 = 0.40$, are provided in figure 25. These visualizations indicate a generally high perturbation level inside the boundary layer. The perturbations are relatively short in the streamwise direction and hence clearly differ from typical boundary-layer streaks.

6.2. *Variation of the forcing waveform*

A generalization of the wall forcing to arbitrary, but nonetheless time-periodic, waveforms has been undertaken by Cimarelli *et al.* (2013) in the context of fully turbulent channel flow. At the optimal parameters, sinusoidal forcing outperformed all other investigated waveforms. If the forcing parameters deviated from their global

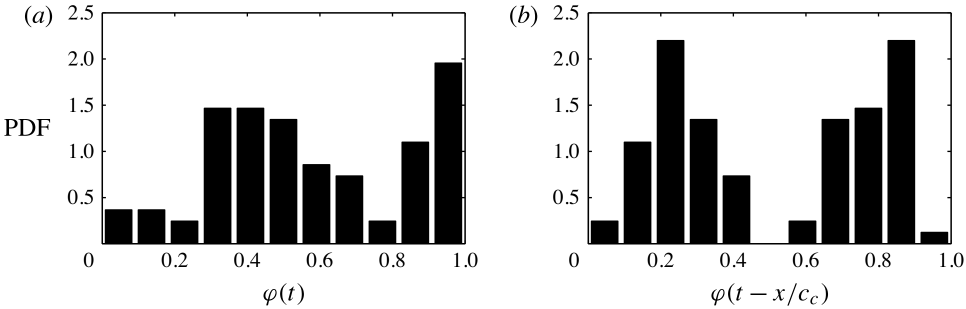

FIGURE 24. PDFs of the phase of spot inception. (*a*) Uncorrected phase, $\varphi(t)$. (*b*) Corrected phase, $\varphi(t-x/c_c)$.

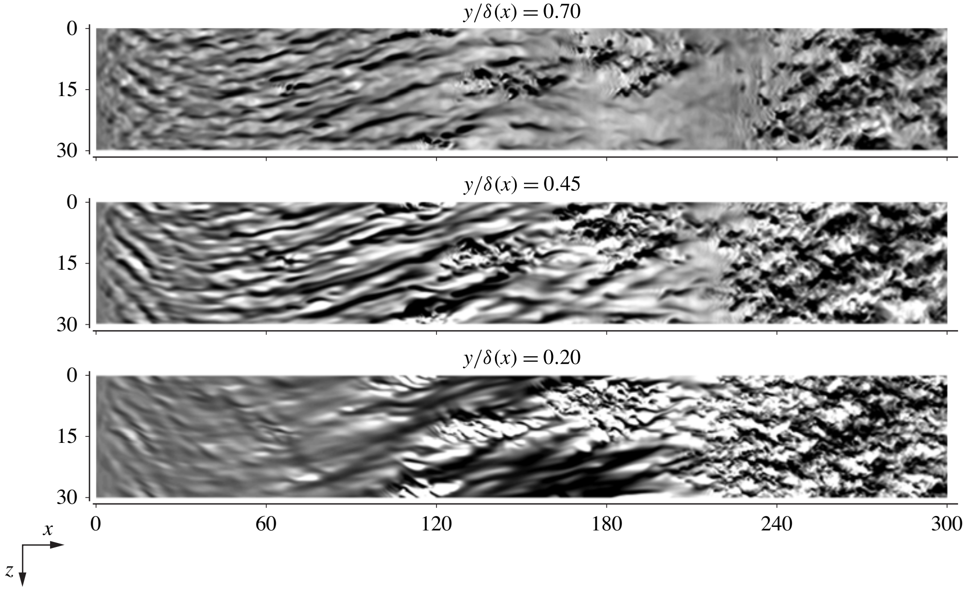

FIGURE 25. Top views, forcing with $T=200$, $W_0=0.40$. Fluctuation of the streamwise velocity component, $-0.10 \leqslant u' \leqslant 0.10$.

optimum, however, other forcing waveforms yielded better performance. For sinusoidal forcing, the time dependence of the shear angle,

$$\psi_\tau \equiv \arctan\left(\frac{\partial W}{\partial y}\bigg/\frac{\partial U}{\partial y}\right),$$

in planes parallel to the wall is also sinusoidal, and there exist intervals of slowly varying ψ_τ (see figure 26*a*). In their investigation of fully turbulent channel flow, Touber & Leschziner (2012) remarked upon the importance of this state of lingering shear strain. They asserted that the very slow reorientation of the shear during phases of lingering allows turbulent streaks sufficient time to amplify in the instantaneous direction of the shear-strain vector. Touber & Leschziner (2012) concluded that drag reduction is undermined if the duration of the lingering state exceeds the time span for the generation of streaks.

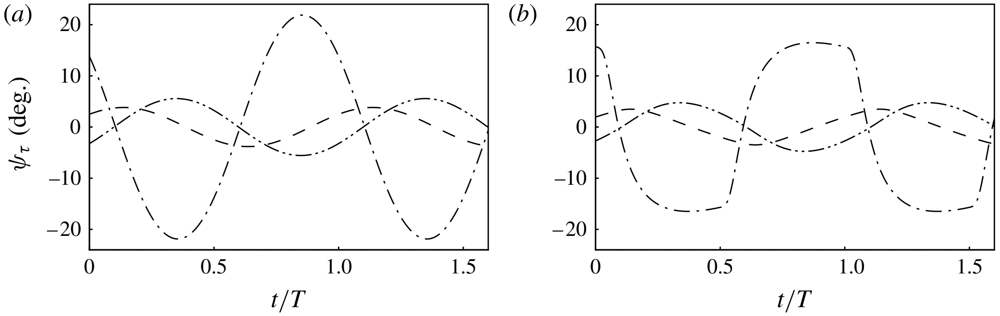

FIGURE 26. Shear angle ψ_τ versus the phase of the base flow at $x = 170$ and $y/\delta(x) = 0.20$ (dashed-dotted), $y/\delta(x) = 0.45$ (dashed) and $y/\delta(x) = 0.70$ (dashed-double dotted). (*a*) Sine wave. (*b*) Square wave.

Additional flow simulations with triangle and square waveforms for the wall velocity were performed, and their influence on transition was determined. A continuously differentiable expression for the triangle wave is given by the Fourier series

$$W_{triangle}(y=0,t) = \frac{8}{\pi^2}\sum_{k=0}^{\infty}\frac{(-1)^k}{(2k+1)^2}\sin\left((2k+1)\frac{2\pi}{T}t\right), \tag{6.2}$$

from which the first 16 terms were retained. A graphical representation of this approximation is given by the dashed-dotted line in figure 27. A Fourier expansion of the square wave, on the other hand, suffers from Gibbs oscillations. Therefore, the square wave was instead approximated by the following C^1 differentiable form,

$$W_{square}(y=0,t) = \begin{cases} W_0 \sin\left(2\pi\dfrac{t}{4a}\right), & 0 < t \leqslant a, \\ W_0, & a < t < T/2 - a, \\ W_0 \sin\left(2\pi\left(\dfrac{1}{2} - \dfrac{T}{8a} + \dfrac{t}{4a}\right)\right), & T/2 - a \leqslant t \leqslant T/2 + a, \\ -W_0, & T/2 + a < t < T - a, \\ W_0 \sin\left(2\pi\left(1 - \dfrac{T}{4a} + \dfrac{t}{4a}\right)\right), & T - a \leqslant t \leqslant T, \end{cases} \tag{6.3}$$

where the constant a is small compared to the oscillation period, $a = 0.02T$. The resulting wall-oscillation profile is shown as the dashed-double dotted line in figure 27, and the shear angle is provided in figure 26(*b*). At $y/\delta(x) = 0.20$, the behaviour of ψ_τ still resembles the square wave at the wall. For larger wall distances, the phase dependence of the shear angle approaches a sine wave.

The forcing amplitudes were chosen such that the power requirements in the laminar region are in all cases equal to that of the sinusoidal forcing. The respective amplitudes and r.m.s. of the spanwise velocity at the wall are provided in table 1.

Flow simulations were performed for all three forcing profiles and an oscillation period $T = 200$. All other parameters, including those of the free-stream turbulence at the inlet were unchanged. The skin friction coefficient is plotted in figure 28(*a*), and demonstrates that forcing with the triangle wave yields nearly identical results to the

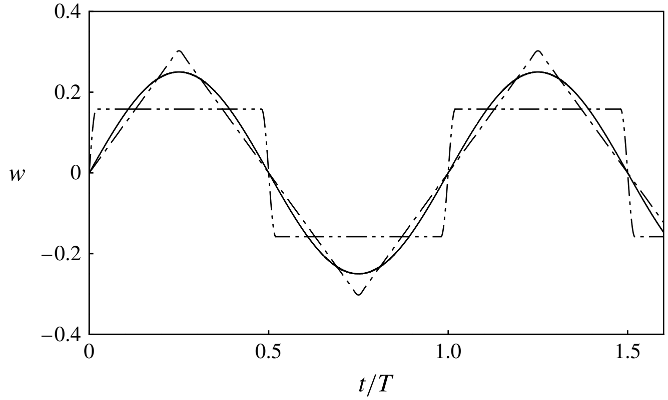

FIGURE 27. Spanwise velocity component at the wall, $w(0, t)$, normalized to identical forcing power requirement, $\overline{P_{forcing}}$: sine wave (solid), triangle wave (dash-dotted) and square wave (dash-double dotted).

	W_0	$w_{rms}(y=0)$
Sine	0.250	0.178
Triangle	0.302	0.188
Square	0.186	0.165

TABLE 1. Properties of forcing waveforms for identical power input, $\overline{P_{forcing}}$.

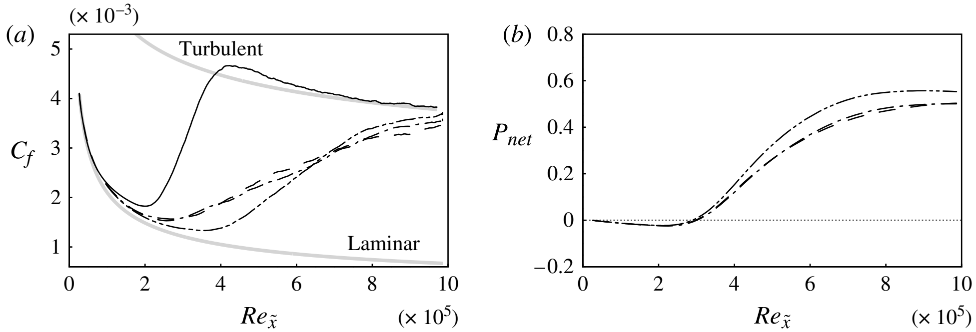

FIGURE 28. Variation of the forcing waveform: reference simulation (solid); sine wave (dashed); triangle wave (dash-dotted); square wave (dash-double dotted). (*a*) Skin friction coefficient C_f over downstream Reynolds number $Re_{\tilde{x}}$. (*b*) Net energetic advantage $\overline{P_{net}}$ over downstream Reynolds number $Re_{\tilde{x}}$.

sinusoidal oscillation. Application of the square wave, on the other hand, preserves laminar flow farther downstream, up to $Re_{\tilde{x}} \approx 3.8 \times 10^5$. The energetic balance is reported in figure 28(*b*). Since the power input is identical in all cases, the net power savings are directly related to the reduction in propulsion power, $\Delta\overline{P_{prop}}$. The downstream shift in transition location in the case of the square wave leads to an increase in $\overline{P_{net}}$ by approximately 20 % at a Reynolds number $Re_{\tilde{x}} \approx 6.2 \times 10^5$.

The results establish that the sudden change of the spanwise velocity in the case of the square wave stabilizes the laminar flow regime more effectively than the sinusoidal forcing. Since the swift change in $W(0, t)$ is the high-frequency part of the wall motion, its influence decays quickly in y, and a sinusoidal time dependence is recovered away from the wall (cf. figure 26). Nearer to the wall, however, the form of the square wave is still discernible and more effectively delays the onset of transition.

The discussion in this section highlights two observations: First, an increase in the oscillation amplitude does not necessarily enhance stability, and can in fact cause transition to shift farther upstream than the reference flow. Second, the sinusoidal wall oscillation did not yield the best performance, for a fixed power input. Both these trends should be compared to the literature on drag reduction in fully turbulent flows where (i) an increase in the amplitude of wall oscillation enhances drag reduction and (ii) the sine wave is the optimal forcing waveform. As such, while the current study was originally motivated by previous work on fully turbulent configurations, the influence of the wall motion on transition is markedly different.

7. Conclusions

The potential to affect bypass breakdown to turbulence via time-harmonic wall forcing was investigated by means of DNS. For suitable forcing parameters, the onset of transition can be shifted downstream appreciably, and the length of the transition region can be significantly extended. It was also demonstrated that the decrease in theoretical propulsion power due to the delay of the fully turbulent flow significantly outweighs the power requirement of the wall forcing.

The transition process is sensitive to the forcing parameters. Starting with very short periods of oscillation, an increase in T enhances drag reduction until an optimum is reached. Longer periods rapidly diminish, and even reverse, the stabilization of the laminar regime. As a result, for periods of approximately twice the optimal value, transition occurs upstream of the unforced reference case. A qualitatively similar behaviour is observed when increasing the amplitude of the forcing beyond its optimal value. Analysis of the phase of spot inception showed that breakdown to turbulence in these cases is correlated with a particular phase of the wall forcing cycle. The focus, however, was placed on the optimal forcing parameters where transition was substantially delayed.

Instantaneous fields and statistical results demonstrated that the optimal oscillation frequency significantly weakened boundary-layer streaks in the pre-transitional flow. Sampling of the properties of large numbers of individual streaks demonstrated that the forcing leads to narrower distributions for the streak amplitudes of both high-speed and low-speed streaks. The averaged amplitudes of laminar streaks are reduced by up to 50 % in comparison to the reference case. In addition, linear stability analyses confirmed a substantial reduction of the growth rates of secondary streak instabilities in the presence of the forcing. These results explain the reduced frequency of occurrence of turbulent spots observed in the DNS.

Finally, a study of different waveforms for the spanwise wall forcing was performed. It was shown that, for identical power input into the wall movement, an oscillation described by a square wave can shift the onset of transition farther downstream than sinusoidal forcing. Apart from the increased efficiency, forcing with a square wave also demands a 40 % lower peak value of the spanwise wall velocity than sinusoidal forcing.

REFERENCES

ANDERSSON, P., BERGGREN, M. & HENNINGSON, D. S. 1999 Optimal disturbances and bypass transition in boundary layers. *Phys. Fluids* **11** (1), 134–150.

ARNAL, D. & MICHEL, R. 1990 *Laminar–Turbulent Transition*, Vol. III. Springer.

BARKLEY, D., BLACKBURN, H. M. & SHERWIN, S. J. 2008 Direct optimal growth analysis for timesteppers. *Intl J. Numer. Meth. Fluids* **57**, 1435–1458.

BARON, A. & QUADRIO, M. 1996 Turbulent drag reduction by spanwise wall oscillations. *Appl. Sci. Res.* **55**, 311–326.

BLACKBURN, H. M. & SHERWIN, S. J. 2004 Formulation of a Galerkin spectral element–Fourier method for three-dimensional incompressible flows in cylindrical geometries. *J. Comput. Phys.* **197**, 759–778.

BOIKO, A. V., WESTIN, K. J. A., KLINGMANN, B. G. B., KOZLOV, V. V. & ALFREDSSON, P. H. 1994 Experiments in a boundary layer subjected to free stream turbulence. Part 2. The role of TS-waves in the transition process. *J. Fluid Mech.* **281**, 219–245.

BOWLES, R. G. A. & SMITH, F. T. 1995 Short-scale effects on model boundary-layer spots. *J. Fluid Mech.* **295**, 395–407.

BRADSHAW, P. & PONTIKOS, N. S. 1985 Measurements in the turbulent boundary layer on an 'infinite' swept wing. *J. Fluid Mech.* **159**, 105–130.

BRANDT, L., SCHLATTER, P. & HENNINGSON, D. S. 2004 Transition in boundary layers subject to free-stream turbulence. *J. Fluid Mech.* **517**, 167–198.

BREUER, K. S. & HARITONIDIS, J. H. 1990 The evolution of a localized disturbance in a laminar boundary layer. Part 1. Weak disturbances. *J. Fluid Mech.* **220**, 569–594.

BUTLER, K. M. & FARRELL, B. F. 1992 Three-dimensional optimal perturbations in viscous shear flow. *Phys. Fluids* A **4** (8), 1637–1650.

CHOI, K.-S. 2002 Near-wall structure of turbulent boundary layer with spanwise-wall oscillation. *Phys. Fluids* **14** (7), 2530–2542.

CHONG, T. P. & ZHONG, S. 2005 On the three-dimensional structure of turbulent spots. *Trans. ASME: J. Turbomach.* **127**, 545–551.

CIMARELLI, A., FROHNAPFEL, B., HASEGAWA, Y., DE ANGELIS, E. & QUADRIO, M. 2013 Prediction of turbulence control for arbitrary periodic spanwise wall movement. *Phys. Fluids* **25**, 075102.

COSSU, C. & BRANDT, L. 2004 On Tollmien–Schlichting-like waves in streaky boundary layers. *Eur. J. Mech.* (B*/Fluids)* **23**, 815–833.

DONG, M. & WU, X. 2013 On continuous spectra of the Orr–Sommerfeld/Squire equations and entrainment of free-stream vortical disturbances. *J. Fluid Mech.* **732**, 616–659.

DRIVER, D. M. & HEBBAR, S. K. 1987 Experimental study of a three-dimensional, shear-driven, turbulent boundary layer. *AIAA J.* **25** (1), 35–42.

DRYDEN, H. L. 1936 Air flow in the boundary layer near a plate. *NACA Report No.* 562. National Advisory Committee for Aeronautics.

DUCHMANN, A., GRUNDMANN, S. & TROPEA, C. 2013 Delay of natural transition with dielectric barrier discharges. *Exp. Fluids* **54**, 1461.

DURBIN, P. A. & WU, X. 2007 Transition beneath vortical disturbances. *Annu. Rev. Fluid Mech.* **39**, 107–128.

EMMONS, H. W. 1951 The laminar–turbulent transition in a boundary layer: part I. *J. Aeronaut. Sci.* **18** (7), 490–498.

FRANSSON, J. H. M. & ALFREDSSON, P. H. 2003 On the disturbance growth in an asymptotic suction boundary layer. *J. Fluid Mech.* **482**, 51–90.

FRANSSON, J. H. M., BRANDT, L., TALAMELLI, A. & COSSU, C. 2005 Experimental study of the stabilization of Tollmien–Schlichting waves by finite amplitude streaks. *Phys. Fluids* **17**, 054110.

HACK, M. J. P. & ZAKI, T. A. 2012 The continuous spectrum of time-harmonic shear layers. *Phys. Fluids* **24** (3), 034101.

HACK, M. J. P. & ZAKI, T. A. 2014 Streak instabilities in boundary layers beneath free-stream turbulence. *J. Fluid Mech.* **741**, 280–315.

HANSON, R. E., BADE, K. M., BELSON, B. A., LAVOIE, P., NAGUIB, A. M. & ROWLEY, C. W. 2014 Feedback control of slowly-varying transient growth by an array of plasma actuators. *Phys. Fluids* **26**, 024102.

HERBERT, T. 1988 Secondary instability of boundary layers. *Annu. Rev. Fluid Mech.* **20**, 487–526.

HUANG, J.-C. & JOHNSON, M. W. 2007 The influence of compliant surfaces on bypass transition. *Exp. Fluids* **42**, 711–718.

HUNT, J. C. R. & CARRUTHERS, D. J. 1990 Rapid distortion theory and the 'problems' of turbulence. *J. Fluid Mech.* **212**, 497–532.

HUNT, J. C. R. & DURBIN, P. A. 1999 Perturbed vortical layers and shear sheltering. *Fluid Dyn. Res.* **24**, 375–404.

JACOBS, R. G. & DURBIN, P. A. 1998 Shear sheltering and the continuous spectrum of the Orr–Sommerfeld equation. *Phys. Fluids* **10** (8), 2006–2011.

JACOBS, R. G. & DURBIN, P. A. 2001 Simulations of bypass transition. *J. Fluid Mech.* **428**, 185–212.

JUNG, W. J., MANGIAVACCHI, N. & AKHAVAN, R. 1992 Suppression of turbulence in wall-bounded flows by high-frequency spanwise oscillations. *Phys. Fluids* A **4** (8), 1605–1607.

KARNIADAKIS, G. E. & CHOI, K.-S. 2003 Mechanisms on transverse motions in turbulent wall flows. *Annu. Rev. Fluid Mech.* **35**, 45–62.

KENDALL, J. 1985 Experimental study of disturbances produced in a pre-transitional laminar boundary layer by weak freestream turbulence. *AIAA Paper* 85-1695.

KERSCHEN, E. J. 1991 Linear and nonlinear receptivity to vortical free-stream disturbances. In *Boundary Layer Stability and Transition to Turbulence* (ed. D. Reda, H. Reed & R. Kobayashi), ASME Fluid Engineering Division Conference, vol. 114, p. 43. ASME.

KIM, J. & MOIN, P. 1985 Application of a fractional-step method to incompressible Navier–Stokes equations. *J. Comput. Phys.* **59**, 308–323.

KLEBANOFF, P. S. 1971 Effect of freestream turbulence on the laminar boundary layer. *Bull. Am. Phys. Soc.* **16**, 1323–1334.

KLEBANOFF, P. S., TIDSTROM, K. D. & SARGENT, L. M. 1962 The three-dimensional nature of boundary layer instability. *J. Fluid Mech.* **12** (1), 1–34.

KLEISER, L. & ZANG, T. A. 1991 Numerical simulation of transition in wall-bounded shear flows. *Annu. Rev. Fluid Mech.* **23**, 495–537.

KURIAN, T. & FRANSSON, J. H. M. 2009 Grid-generated turbulence revisted. *Fluid Dyn. Res.* **41**, 021403.

LANDAHL, M. T. 1975 Wave breakdown and turbulence. *SIAM J. Appl. Maths* **28** (4), 735–756.

LANDAHL, M. T. 1980 A note on an algebraic instability of inviscid parallel shear flows. *J. Fluid Mech.* **98**, 243–251.

LARDEAU, S. & LESCHZINER, M. A. 2013 The streamwise drag-reduction response of a boundary layer subjected to a sudden imposition of transverse oscillatory wall motion. *Phys. Fluids* **25**, 075109.

LEIB, S. J., WUNDROW, D. W. & GOLDSTEIN, M. E. 1999 Effect of free-stream turbulence and other vortical disturbances on a laminar boundary layer. *J. Fluid Mech.* **380**, 169–203.

LIU, Y., ZAKI, T. A. & DURBIN, P. A. 2008*a* Boundary-layer transition by interaction of discrete and continuous modes. *J. Fluid Mech.* **604**, 193–233.

LIU, Y., ZAKI, T. A. & DURBIN, P. A. 2008*b* Floquet analysis of secondary instability of boundary layers distorted by Klebanoff streaks and Tollmien–Schlichting waves. *Phys. Fluids* **20**, 124102.

MALIK, S. V. & HOOPER, A. P. 2005 Linear stability and energy growth of viscosity stratified flows. *Phys. Fluids* **17**, 024101.

MANDAL, A. C., VENKATAKRISHNAN, L. & DEY, J. 2010 A study on boundary-layer transition induced by free-stream turbulence. *J. Fluid Mech.* **660**, 114–146.

MATSUBARA, M. & ALFREDSSON, P. 2001 Disturbance growth in boundary layers subjected to free-stream turbulence. *J. Fluid Mech.* **430**, 149–168.

MOIN, P., SHIH, T.-H., DRIVER, D. & MANSOUR, N. N. 1990 Direct numerical simulation of a three-dimensional turbulent boundary layer. *Phys. Fluids* **2** (10), 1846–1853.

NAGARAJAN, S., LELE, S. K. & FERZIGER, J. H. 2007 Leading-edge effects in bypass transition. *J. Fluid Mech.* **572**, 471–504.

NOLAN, K. P. & ZAKI, T. A. 2013 Conditional sampling of transitional boundary layers in pressure gradients. *J. Fluid Mech.* **728**, 306–339.

OVCHINNIKOV, V., CHOUDHARI, M. M. & PIOMELLI, U. 2008 Numerical simulations of boundary-layer bypass transition due to high-amplitude free-stream turbulence. *J. Fluid Mech.* **613**, 135–169.

PHILLIPS, O. M. 1969 Shear-flow turbulence. *Annu. Rev. Fluid Mech.* **1**, 245–264.

QUADRIO, M. & RICCO, P. 2004 Critical assessment of turbulent drag reduction through spanwise wall oscillations. *J. Fluid Mech.* **521**, 251–271.

QUADRIO, M., RICCO, P. & VIOTTI, C. 2009 Streamwise-travelling waves of spanwise wall velocity for turbulent drag reduction. *J. Fluid Mech.* **627**, 161–178.

RICCO, P. 2011 Laminar streaks with spanwise wall forcing. *Phys. Fluids* **22**, 064103.

ROACH, P. & BRIERLEY, B. 1990 The influence of a turbulent freestream on zero pressure gradient transitional boundary layer development, Part I: Test cases T3A and T3B. In *ERCOFTAC Workshop: Numerical Simulation of Unsteady Flows and Transition to Turbulence, Lausanne, Switzerland*, pp. 319–347. Cambridge University Press.

ROSENFELD, M., KWAK, D. & VINOKUR, M. 1991 A fractional step solution method for the unsteady incompressible Navier–Stokes equations in generalized coordinate systems. *J. Comput. Phys.* **94**, 102–137.

SAMEEN, A. & GOVINDARAJAN, R. 2007 The effect of wall heating on instability of channel flow. *J. Fluid Mech.* **577**, 417–442.

SARIC, W. S., REED, H. L. & KERSCHEN, E. J. 2002 Boundary-layer receptivity to freestream disturbances. *Annu. Rev. Fluid Mech.* **34**, 291–319.

SCHRADER, L.-U., BRANDT, L. & HENNINGSON, D. S. 2009 Receptivity mechanisms in three-dimensional boundary-layer flows. *J. Fluid Mech.* **618**, 209–241.

SCHRADER, L.-U., SUBIR, A. & BRANDT, L. 2010 Transition to turbulence in the boundary layer over a smooth and rough swept plate exposed to free-stream turbulence. *J. Fluid Mech.* **646**, 297–325.

SORENSEN, D. C. 1992 Implicit application of polynomial filters in a k-step Arnoldi method. *SIAM J. Matrix Anal. Applics.* **13** (1), 357–385.

SPALART, P. R. 1989 Theoretical and numerical study of a three-dimensional turbulent boundary layer. *J. Fluid Mech.* **205**, 319–340.

SUDER, K. L., O'BRIEN, J. E. & RESHOTKO, E. 1981 Experimental study of bypass transition in a boundary layer. *NASA Rep.* TM-100913. National Aeronautics and Space Administration.

TAYLOR, G. I. 1939 Some recent developments in the study of turbulence. In *Proceedings of the 5th International Congress for Applied Mechanics* (ed. J. Den Hartog & H. Peters), pp. 294–310. Wiley.

TOUBER, E. & LESCHZINER, M. A. 2012 Near-wall streak modification by spanwise oscillatory wall motion and drag-reduction mechanisms. *J. Fluid Mech.* **507**, 1–51.

VAUGHAN, N. J. & ZAKI, T. A. 2011 Stability of zero-pressure-gradient boundary layer distorted by unsteady Klebanoff streaks. *J. Fluid Mech.* **681**, 116–153.

VIOTTI, C., QUADRIO, M. & LUCHINI, P. 2009 Streamwise oscillation of spanwise velocity at the wall of a channel for turbulent drag reduction. *Phys. Fluids* **21**, 115109.

WHITE, F. M. 2005 *Viscous Fluid Flow*, 3rd edn. McGraw-Hill.

WYGNANSKI, I., SOKOLOV, M. & FRIEDMAN, D. 1976 On a turbulent 'spot' in a laminar boundary layer. *J. Fluid Mech.* **78**, 785–819.

ZAKI, T. A. 2013 From streaks to spots and on to turbulence: exploring the dynamics of boundary layer transition. *Flow Turbul. Combust.* **91**, 451–473.

ZAKI, T. A. & DURBIN, P. A. 2005 Mode interaction and the bypass route to transition. *J. Fluid Mech.* **531**, 85–111.

ZAKI, T. A. & SAHA, S. 2009 On shear sheltering and the structure of vortical modes in single- and two-fluid boundary layers. *J. Fluid Mech.* **626**, 111–147.